HHS Public Access

Author manuscript

Nature. Author manuscript; available in PMC 2020 May 27.

Published in final edited form as:

Nature. 2019 December ; 576(7786): 315–320. doi:10.1038/s41586-019-1795-x.

Structure and Drug Resistance of the *Plasmodium falciparum* Transporter PfCRT

Jonathan Kim[1,11], **Yong Zi Tan**[1,2,11], **Kathryn J. Wicht**[3,12], **Satchal K. Erramilli**[4,12], **Satish K. Dhingra**[3], **John Okombo**[3], **Jeremie Vendome**[5], **Laura M. Hagenah**[3], **Sabrina I. Giacometti**[1], **Audrey L. Warren**[6], **Kamil Nosol**[4], **Paul D. Roepe**[7], **Clinton S. Potter**[2,8], **Bridget Carragher**[2,8], **Anthony A. Kossiakoff**[4], **Matthias Quick**[6,9,*], **David A. Fidock**[3,10,*], **Filippo Mancia**[1,*]

[1]Department of Physiology and Cellular Biophysics, Columbia University Irving Medical Center, New York, NY 10032, USA.

[2]National Resource for Automated Molecular Microscopy, Simons Electron Microscopy Center, New York Structural Biology Center, New York, NY 10027, USA.

[3]Department of Microbiology and Immunology, Columbia University Irving Medical Center, New York, NY 10032, USA.

[4]Department of Biochemistry and Molecular Biology, University of Chicago, Chicago, IL 60637, USA.

[5]Schrödinger, Inc., New York, NY 10036, USA.

[6]Department of Psychiatry, Center for Molecular Recognition, Columbia University Irving Medical Center, New York, NY 10032, USA.

[7]Department of Chemistry and Department of Biochemistry and Cellular and Molecular Biology, Georgetown University, Washington DC, 20057, USA.

[8]Department of Biochemistry and Molecular Biophysics, Columbia University Irving Medical Center, New York, NY 10032, USA.

[9]Division of Molecular Therapeutics, New York State Psychiatric Institute, New York, NY 10032, USA.

*Correspondence to be addressed to: mq2102@cumc.columbia.edu (MQ); df2260@cumc.columbia.edu (DAF); fm123@cumc.columbia.edu (FM).

Correspondence and requests for materials should be addressed to M.Q., D.A.F., or F.M.

Author contributions J.K. with help from L.M.H. and S.I.G performed protein expression and purification. S.K.E., K.N., and A.A.K. identified the Fabs. Y.Z.T. and J.K. produced and analyzed the cryo-EM data, and built the model, with help from B.C. and C.S.P. M.Q. and A.L.W. performed the biochemical assays. K.J.W., S.K.D., J.O., P.D.R. and D.A.F. conducted mutational analyses. K.J.W. and J.V. performed computational studies, and S.K.D. and J.O. performed parasite gene editing and characterization. M.Q., D.A.F. and F.M. designed experiments and wrote the paper with J.K., Y.Z.T., K.J.W., and P.D.R.

Competing interests: The authors declare no competing interest.

Data availability: All raw movie frames, micrographs, the particle stack and relevant metadata files have been deposited into EMPIAR, with accession code EMPIAR-10330. The electron density map has been deposited into EMDB, with accession code EMD-20806. The model has been deposited in the PDB, with accession code 6UKJ. All data are available in the manuscript or the supplementary materials.

[10]Division of Infectious Diseases, Department of Medicine, Columbia University Irving Medical Center, New York, NY 10032, USA.

[11]These authors contributed equally.

[12]These authors contributed equally.

Summary

The emergence and spread of drug-resistant *Plasmodium falciparum* impedes global efforts to control and eliminate malaria. For decades, treatment relied on chloroquine (CQ), a safe and affordable 4-aminoquinoline that was highly effective against intra-erythrocytic asexual blood-stage parasites, until resistance arose in Southeast Asia and South America and spread worldwide[1]. Clinical resistance to the chemically-related current first-line combination drug piperaquine (PPQ) has now emerged regionally, thwarting its efficacy[2]. Resistance to CQ and PPQ has been associated with distinct sets of point mutations in the *P. falciparum* chloroquine resistance transporter PfCRT, a 49 kDa member of the drug/metabolite transporter (DMT) superfamily that traverses the membrane of the parasite's acidic digestive vacuole (DV)[3–9]. Here we present the 3.2 Å structure of the PfCRT isoform from CQ-resistant, PPQ-sensitive South American 7G8 parasites, using single-particle cryo-electron microscopy (cryo-EM) and fragment antigen-binding (Fab) technology. Mutations contributing to CQ and PPQ resistance localize primarily to moderately-conserved sites on distinct helices lining a central negatively-charged cavity, implicating this as the principal site of interaction with positively-charged CQ and PPQ. Binding and transport studies reveal that the 7G8 isoform binds both drugs with comparable affinities, with these drugs being mutually competitive. This isoform transports CQ in a membrane potential- and pH-dependent manner, consistent with an active efflux mechanism driving CQ resistance[5], but does not transport PPQ. Functional studies on the newly emerging PfCRT F145I and C350R mutations, associated with decreased PPQ susceptibility in Asia and South America respectively[6,9], reveal their ability to mediate PPQ transport in 7G8 variant proteins and to confer resistance in gene-edited parasites. Structural, functional and *in silico* analyses suggest distinct mechanistic features mediating CQ and PPQ resistance in PfCRT variants. These data provide the first atomic-level insights into the molecular mechanism of this key mediator of antimalarial treatment failures.

Keywords

Malaria; resistance; chloroquine; piperaquine; structural biology; membrane transport; single-particle cryo-electron microscopy; antibody phage display

---

Recent reductions in the global malaria burden have stalled, with the situation in Southeast Asia exacerbated by emerging resistance to artemisinin-based combination therapies including the bis-4-aminoquinoline partner drug PPQ[10]. A major determinant of drug resistance in malaria parasites is the *P. falciparum* transporter PfCRT[5]. Amino acid substitutions in this protein comprise haplotypes that originated independently decades ago in several regions subjected to intense drug pressure with CQ, the former gold-standard antimalarial. These include the 5-amino acid 7G8 variant that dominates in South America and the Western Pacific, and the 8-amino acid Dd2 variant that is prevalent in Southeast Asia

(Extended Data Fig. 1). Recent extensive use of PPQ in Cambodia is suspected to have driven the rapid emergence of novel PfCRT mutations, arising on the Dd2 isoform[6–8]. These mutations have become widespread across Southeast Asia, where they are associated with dihydroartemisinin-PPQ treatment failures that now average 50% in the region and reach 87% in northeastern Thailand[2,7]. CQ and PPQ are thought to act by accumulating in the intra-erythrocytic parasite's acidic DV as protonated species (CQ^{2+} and PPQ^{4+}). These drugs bind toxic Fe^{3+}-heme, released from proteolysed host hemoglobin, and inhibit heme incorporation into chemically inert hemozoin[11,12]. Resistance to CQ has been attributed to mutant PfCRT-mediated drug efflux out of the DV (Fig. 1a)[4,13–16], whereas the mechanism of PPQ resistance has remained enigmatic.

We used single-particle cryo-EM to determine the structure of the 49 kDa PfCRT 7G8 isoform, identified as the most suitable candidate from a panel of 12 sequence variants and/or orthologs expressed in HEK-293 cells. To overcome current cryo-EM size limitations[17], we screened a synthetic phage display library[18] to select for recombinant PfCRT-specific antigen-binding fragments (Fabs, ~50 kDa). PfCRT complexes were obtained with several candidates, including the CTC Fab that yielded high-quality 2D class averages obtained by negative-stain EM (Extended Data Fig. 2).

We solved the structure of the nanodisc-incorporated PfCRT 7G8-Fab CTC complex to a nominal resolution of 3.3 Å, with the PfCRT portion resolved to 3.2 Å (Extended Data Table 1; Extended Data Fig. 3). We built a *de novo* model of PfCRT comprising residues 47–113 and 123–405 of the 424-amino acid protein (Fig. 1b, c). PfCRT appears monomeric and consists of 10 transmembrane (TM) helices (Fig. 1b). Two juxtamembrane helices (JM1 and JM2), parallel to and on opposite sides of the DV membrane, are located at the cytosolic N-terminus and between TM helices 7 and 8, respectively (Fig. 1b, c; Extended Data Fig. 4). The 10 TMs are arranged as five helical pairs that form two-helix hairpins with an inverted antiparallel topology (Extended Data Fig. 5a). TM helices 1–4 and 6–9 form a central cavity of ~3,300 $Å^3$ that is wider on the DV side and closes approximately halfway into the membrane, suggesting that the structure is in an open-to-DV/inward-open conformation (Fig. 1b, d). The pseudo-symmetrical arrangement of the TM helices also enabled us to model the alternative open-to-cytosol conformation of TM helices 1–10 (Extended Data Fig. 5b).

Structural conservation of PfCRT 7G8 with solved structures of several DMT superfamily members is high in the TM helices, with 2.8–4.0 Å average distances between backbone atoms (Extended Data Fig. 5c). The central cavity in the structurally-conserved DMT proteins constitutes the known ligand-binding site (Extended Data Fig. 5d), suggesting this cavity as the likely equivalent site in PfCRT. The net charge in the PfCRT 7G8 cavity is negative (Fig. 1d; Extended Data Fig. 5d), influenced mainly by D137, D326 and D329 (Extended Data Fig. 6a), suggesting that putative substrates for PfCRT 7G8 are likely positively charged. Consistent with this proposal, the positively-charged R111 residue in the variable loop region of the Fab CTC protrudes into the PfCRT cavity (Extended Data Fig. 6a). Interactions between Fab R111 and PfCRT D326 and D329 presumably help stabilize the PfCRT 7G8-Fab complex. We also identified density in a separate hydrophobic cleft, delineated by JM1, TM1, TM9 and TM10, unique to PfCRT and near the cytosolic side of

the DV membrane. We tentatively assigned this to cholesteryl hemisuccinate, present during the purification (Extended Data Fig. 6b–d).

The PfCRT central cavity, with a ~25Å maximum diameter, is in principle able to accommodate CQ or PPQ (~14 and ~21Å maximum lengths, respectively; Extended Data Fig. 6e). All CQ-resistant (CQ-R) isoforms, irrespective of geographic origin, share a common and requisite K76T mutation[13,19], which our structure places directly in the lining of the cavity (Fig. 2). Compared with the canonical wild-type (WT) CQ-sensitive (CQ-S) 3D7 isoform, the CQ-R 7G8 isoform has four additional mutations (C72S, A220S, N326D, I356L) that also line the cavity (Fig. 2; Extended Data Table 2a). Similarly, the CQ-R Dd2 isoform has six of its eight mutations (M74I, N75E, K76T, A220S, N326S, I356T) located within the cavity, with two additional mutations (Q271E and R371I) located at its entrance (Fig. 2). Distinct amino acid substitutions associated with PPQ-R also line the cavity, including C350R that arose on the 7G8 isoform, and H97Y, F145I and G353V, as well as the recently described mutations T93S and I218F, which each emerged separately on the Dd2 isoform[2,6–9] (Fig. 2; Extended Data Table 2a). M343L, which confers low-grade PPQ resistance in the Dd2 isoform[6], lies above, close to the cytosol (Fig. 2).

CQ resistance-associated mutations are confined mostly to a single region involving TM helices 1, 6, 8 and 9, contrasting with the PPQ mutations that are positioned primarily in two distinct regions involving TM helices 2, 3, 6 and 9 (Extended Data Fig. 6f). All PPQ-R point mutations arose individually on the CQ-R Dd2 or 7G8 isoforms, indicating that the interaction with the larger and more positively charged PPQ^{4+} requires additional modifications to the central cavity. Potentially, the physical separation between the sets of mutated helices in the PPQ-R isoforms might correlate with PPQ's two 4-aminoquinoline ring structure, contrasting with the pattern observed for CQ that contains one 4-aminoquinoline ring (Extended Data Fig. 6e, f). No PfCRT mutations associated with resistance to either drug mapped to residues that were fully conserved across our set of Apicomplexan CRT orthologs (Extended Data Fig. 6f, 7; Extended Data Table 2a), suggesting structural and/or functional constraints. Resistance-conferring mutations map to moderately conserved sites in select helices, in residues lining the cavity, thus providing a road map of sites for future PPQ resistance surveillance. For example, residues with these properties on TM2 are at positions 90, 93, 94, 97, 98 and 101, amongst which T93S, H97Y and C101F have each been associated with PPQ resistance[6–8,12]. In contrast, mutations earlier found in Southeast Asia that have not recently expanded in areas of PPQ treatment include L196P, N295I, A366T and G367C, which do not meet the above criteria[6,7].

To translate structural observations into transporter function, we first used purified protein in scintillation proximity-based assays (SPA) to measure drug binding[20]. Results with PfCRT 7G8 reconstituted in nanodiscs showed binding to CQ and PPQ, at comparable levels (Fig. 3a). Isotopic dilution assays yielded mean half-maximal binding constants (EC_{50} values) of ~300 nM for CQ, similar to earlier studies with Dd2 PfCRT[21], and ~190 nM for PPQ (Fig. 3b). Each drug competitively inhibited binding of the other with virtually identical mean half-maximal inhibition constants (IC_{50} values) of ~170 nM (Fig. 3c).

Binding of these two drugs was partially inhibited by verapamil (Fig. 3d), a known CQ resistance reversal agent[22]. Near-complete inhibition was observed with amodiaquine, a related 4-aminoquinoline first-line partner drug against which PfCRT 7G8 mediates cross resistance[23]. Control assays found no inhibition of [^{3}H]-CQ or [^{3}H]-PPQ binding with the chemically distinct antimalarials lumefantrine and atovaquone that have separate modes of action[5].

We also observed inhibition of [^{3}H]-CQ and [^{3}H]-PPQ binding with excess arginine, consistent with the observed interaction between the Fab R111 and the PfCRT cavity (Extended Data Fig. 6a), and prior [^{3}H]-Arg transport studies[25]. Control experiments revealed no inhibition of drug binding with the neutral amino acid leucine (Fig. 3d). SPA results showed binding of [^{3}H]-Arg to PfCRT 7G8 with a half-maximal binding constant of ~400 μM (Extended Data Fig. 8a, b). This binding was effectively competed by both CQ and PPQ, as well as by amodiaquine and non-radiolabeled arginine or lysine, but not by leucine (Extended Data Fig. 8c). Binding of [^{3}H]-Arg, [^{3}H]-CQ and [^{3}H]-PPQ was inhibited by the Fab in a concentration-dependent manner (Fig. 3e), suggesting overlapping binding of Arg, CQ, PPQ and the Fab to the PfCRT cavity.

We next showed that active [^{3}H]-CQ and [^{3}H]-Arg uptake required an inwardly directed pH gradient (pH 5.5–7.5, corresponding to the parasite DV pH gradient[26]), and a membrane potential $\Delta\Psi$ (Extended Data Fig. 8d). Here, $\Delta\Psi$ was created by using the K^+-specific ionophore valinomycin to generate an outward-directed K^+ diffusion gradient from the proteoliposomes. Under these conditions, [^{3}H]-CQ and [^{3}H]-Arg uptake was maximal within one minute (Fig. 3f). Kinetic characterization of concentration-dependent [^{3}H]-CQ and [^{3}H]-Arg uptake yielded Michaelis-Menten constants (K_m) of 0.8 μM and 1.3 μM and maximum velocities of transport (V_{max}) of ~90 nmol x mg^{-1} x min^{-1} and 190 nmol x mg^{-1} x min^{-1}, respectively (Fig. 3f, *inset*). Assuming full activity of PfCRT 7G8 reconstituted in proteoliposomes, these V_{max} values reflect catalytic turnover numbers (k_{cat}) of ~ 0.2 s^{-1} and ~0.4 s^{-1}, respectively, values that are characteristic for secondary active transporters rather than for channels[27]. Collectively, these results support proton motive force-dependent CQ efflux as the mechanism underlying mutant PfCRT 7G8-mediated CQ resistance, in agreement with earlier reports[4,13–15,22]. Under our experimental conditions, no detectable [^{3}H]-PPQ uptake was observed with PfCRT 7G8 in proteoliposomes, as expected for this PPQ-sensitive (PPQ-S) isoform (Fig. 3f). We also observed partial to strong inhibition of [^{3}H]-CQ and [^{3}H]-Arg uptake by verapamil and 4-aminoquinolines, further implicating a crucial role for the central cavity in substrate recognition (Fig. 3g; Extended Data Fig. 8e).

Our structural analysis reveals four cysteines in the long loop between TM helices 7 and 8, located on the DV side near the entrance to the cavity. These cysteines, which appear to form the disulfide bridges Cys289-Cys312 and Cys301-Cys309 (located next to JM2 and at the tip of the loop, respectively), are absolutely conserved (Extended Data Fig. 7, 9a), suggesting a potential redox-dependent mechanistic role. Of note, *P. falciparum* intra-erythrocytic parasites are subjected to oxidative stress during parasite-mediated hemoglobin proteolysis and Fe^{2+}-heme oxidation[5]. We expressed and purified 7G8 variants that harbored either a C301A or C289A mutation. We observed equivalent [^{3}H]-CQ binding for these variants and 7G8, which was unaffected by increasing concentrations of the reducing agent β

−mercaptoethanol (β-MeOH; Extended Data Fig. 9b). [^{3}H]-CQ uptake was also similar between these three isoforms in the absence of reducing agent. Increasing the concentration of β-MeOH led to reduced CQ uptake, with 7G8 and 7G8+C301A differing in their dose-dependency (Extended Data Fig. 9c), consistent with a possible role of Cys289-Cys312 in regulating CQ transport.

To relate PfCRT structure and function to resistance mechanisms, we leveraged mutations in Dd2 and 7G8 isolates implicated in differential CQ and PPQ susceptibilities. We chose the F145I mutation, which mediates high-grade resistance to PPQ in Dd2 parasites and which is associated with a significantly increased risk of DHA-PPQ treatment failure in Southeast Asia[2,6,7,28]. We hypothesized that this mutation might also afford PPQ resistance on the 7G8 (South American and Western Pacific) background. We also selected the C350R mutation, found in in 7G8 parasites and earlier proposed to have arisen from local PPQ drug pressure[9].

First, we expressed recombinant PfCRT variants 7G8, 7G8+F145I, 7G8+C350R and Dd2, as well as the canonical CQ-S and PPQ-S WT isoform (from 3D7 parasites). These purified proteins were reconstituted in nanodiscs and tested in equilibrium dialysis experiments for [^{3}H]-CQ and [^{3}H]-PPQ binding. Results showed a comparable dissociation constant (K_d) across all variants for both drugs at pH 7.5 (Extended Data Table 2b). However, at pH 5.5, which reflects the pH of the acidic DV[26], we observed a ~2-fold increase in the PPQ^{4+} K_d (i.e. a ~2-fold lower binding affinity) for the 7G8+F145I and 7G8+C350R variants when compared with the 7G8 parental isoform (Fig. 3h; Extended Data Table 2b). Testing PPQ uptake in PfCRT proteoliposomes revealed substantially increased PPQ transport rates by the 7G8+F145I and 7G8+C350R variants (Fig. 3i, j; Extended Data Table 2b). Minimal PPQ transport was observed with the PPQ-S isoforms 7G8, Dd2 and WT. Whereas the low transport activity of the 7G8 and Dd2 parental isoforms correlated with the higher PPQ^{4+} binding affinity at pH 5.5 (Fig. 3h), this relationship was not observed for WT (exhibiting a low PPQ^{4+} binding affinity and minimal PPQ transport activity). For CQ, results showed robust transport activity with the CQ-R 7G8 and Dd2 parental isoforms, reduced uptake by the 7G8+F145I and 7G8+C350R variants, and minimal uptake by WT (Fig. 3i). For the 7G8+C350R variant, the higher CQ^{2+} binding affinity (Fig. 3h) paralleled reduced CQ transport (Fig. 3i). However, for the WT protein the low CQ transport activity could not be attributed to tight CQ^{2+} binding that would potentially impede the effective dissociation of the drug from the transporter. In summary, these biochemical data provide evidence that both the F145I and C350R mutations can mediate PPQ efflux when introduced into the 7G8 isoform, concomitant with reduced CQ transport. These data also implicate drug-specific transport, differentially mediated by PfCRT mutations lining distinct sites in the central cavity, as the major determinant of resistance.

To correlate these findings to drug susceptibility in the parasite, we genetically edited *pfcrt* in the *P. falciparum* 7G8 line to express the 7G8+F145I or C350R variants and compared these to control isogenic 7G8 parasites expressing the 7G8 isoform. Their characterization revealed a significant increase in the CQ cellular accumulation ratio (CAR) after 1 h in 7G8+F145I and 7G8+C350R clones, compared to the CQ-R 7G8 and Dd2 lines that showed a minimal CAR (Fig. 3k; Extended Data Table 3). WT (3D7) CQ-S parasites showed high levels of CQ accumulation. For PPQ, the F145I and C350R variants showed a decrease in

the CAR compared to the 7G8 parent, although the difference was smaller than for CQ. PPQ accumulation levels were uniformly high for the PPQ-S 7G8, Dd2 and 3D7 parasites. These CAR data are consistent with parasite 72 h growth inhibition assays that showed reversal of CQ resistance upon introduction of the F145I and C350R mutations into 7G8 parasites, mirrored by increased PPQ IC_{50} and IC_{90} values in these variants (Extended Data Table 3). The 7G8+F145I mutant showed a pronounced biphasic dose-response curve, with IC_{90} values showing a 188-fold increase compared to the isogenic 7G8 control line. A similar fold increase in PPQ IC_{90} values was observed in parallel studies that compared the Dd2+F145I mutant with isogenic Dd2 parasites (Extended Data Fig. 9d). These findings provide evidence that the F145I mutation affords comparable high-grade PPQ resistance at elevated PPQ concentrations in these two genetically and geographically distinct backgrounds (Extended Data Fig. 9d;[6]).

As stated above, PPQ resistance in parasites is evident only at high nanomolar PPQ concentrations[6,29]. Accordingly, PPQ resistance is best examined using PPQ survival assays, in which synchronized ring-stage parasites (0–6 h post-invasion of erythrocytes) are exposed to high concentrations of drug for 48 h and the percent survival is measured 24 h later as a percent of surviving mock-treated parasites[30]. Results from this assay revealed 9–10% survival at the standard assay concentration of 200 nM PPQ, with similar levels of survival maintained at PPQ concentrations of up to 1,600 nM (Fig. 3l; Extended Data Table 3). PPQ-S parasites showed 1% survival or less at concentrations of 200 nM or more. These results agree with our biochemical studies showing increased PPQ transport, accompanied by diminished CQ transport, upon introducing the Asian and South America F145I and C350R mutations respectively into the 7G8 isoform. These findings provide compelling evidence that these novel PfCRT mutations could impact PPQ efficacy in South America.

To link our structural and functional findings, we calculated the electrostatics of the central cavity for the PfCRT isoforms described above. 7G8 and Dd2 exhibit the most electronegativity in the central cavity, consistent with their highest affinity for PPQ at pH 5.5 (Fig. 3h; Extended Data Fig. 10a). Assuming PPQ^{4+} formation at pH 5.5, these variants would feature the strongest electrostatic interaction of PPQ^{4+} in the PfCRT cavity. Introducing an Arg into this cavity (7G8+C350R) caused a reduction in its electronegativity (Extended Data Fig. 10b), which could explain the reduced binding affinity for PPQ and the resulting transport-positive phenotype of this variant (Fig. 3h–j). In the case of PfCRT 7G8+F145I, however, the electrostatic charge in the central cavity appeared unchanged when calculated on the 7G8 model. On the other hand, molecular dynamic simulations suggested a conformational impact of the F145I mutation, involving a substantial displacement of TM1, with 145I (TM3) showing greater atomic distance from L83 (TM1) compared to F145 in 7G8 (Extended Data Fig. 10c). TM7 was also notably displaced towards the 145I variant, as shown by the distance to V263. In contrast, marginal movement was observed with the C350R mutation (Extended Data Fig. 10d). These simulations suggest changes in the cavity shape and size resulting from the F145I mutation that could impact molecular interactions essential for the differential transport of CQ and PPQ.

Our data point to a complex mechanism of resistance that is dependent on the gain of CQ^{2+} or PPQ^{4+} efflux through specific mutations in the central cavity of PfCRT, which evolved

under regional selective drug pressures beginning decades ago with the former first-line drug CQ and more recently involving PPQ. These mutation-specific changes can differentially impact the electrostatic properties of the cavity affecting drug binding and/or the structural dynamics that are associated with transport[24]. The apparent dichotomy observed between CQ and PPQ for the F145I and C350R mutants, which evolved on CQ-R isoforms and caused CQ resensitization along with a gain of PPQ resistance, highlights the value of extending this research to rapidly emerging PfCRT mutations[2,7,8], in order to identify antimalarial combinations that could exert opposing selective pressures on this transporter.

Methods

Small-scale expression screen of CRT variants

Initial expression studies were performed with twelve CRT variants, including the *Plasmodium falciparum crt* sequences 7G8 (AF233064), 3D7 (Q9N623, codon optimized for *Xenopus laevis*), Dd2 (D5L5S2, codon optimized for *Xenopus laevis*), *Plasmodium berghei* CRT (PbCRT, Q9GSD8), *Plasmodium knowlesi* CRT (PkCRT, Q9GSD7), *Plasmodium vivax* CRT (PvCRT, Q9GSD3, codon optimized for *Spodoptera frugiperda*), *Theileria parva* CRT (TpCRT, Q4N5R6), *Theileria annulata* CRT (TaCRT, Q4UDS9), and *Cryptosporidium parvum* CRT (CpCRT, Q7YZ23). To express these in mammalian cells, the sequences were cloned into pFM1.2[31] as a GFP fusion with a decahistidine affinity tag at either the 5’ or 3’ end of the gene. One μg of each construct was diluted into 100 μl opti-MEM (Thermo Fisher Scientific) and mixed with 100 μl opti-MEM containing 4 μg of polyethylenimine (PEI) Max MW 40,000 (Polysciences). This mixture was added to 1.0×10^6 HEK293T cells (Invitrogen) cells in a total volume of 2 ml in a 6-well plate (Corning). The cell transfection mixture was incubated at 37°C for 72 h in 5% CO_2. Transfected cells were then harvested, centrifuged at 800×*g* for 10 min at 4°C, and washed once on ice in 1×PBS. Each pellet was resuspended and solubilized in 20 mM HEPES pH 7.5, 200 mM NaCl, 20 mM $MgSO_4$, 0.5 mM phenylmethylsulfonyl fluoride (PMSF), cOmplete™ EDTA-free Protease Inhibitor Cocktail (Roche), 10 μg/ml DNase I (Roche), and 8 μg/ml RNase (Sigma-Aldrich) supplemented with 1% n-dodecyl-β-D-maltopyranoside (DDM) and 0.1% cholesteryl hemisuccinate (CHS) at 4°C for 2 h. Insoluble material was removed by ultracentrifugation in a single angle rotor at 4°C for 45 min. The supernatant of each sample was subjected to western blot analysis using a rabbit anti-GFP antibody (diluted 1:5,000; Invitrogen) and a secondary goat anti-rabbit IgG conjugated to horseradish peroxidase (diluted 1:7,000; Invitrogen). Labeling was detected using a western blot Luminol reagent (Santa Cruz).

Expression and stability were further evaluated by fluorescence-coupled size exclusion chromatography (FSEC)[32]. In these assays, each GFP-tagged construct was transfected into HEK293 Freestyle cells (Invitrogen) in the presence of PEI. Transfected cells were incubated at 37°C for 72 h with 8% CO_2 and 70% humidity. Cell supernatants were prepared for FSEC analysis as described above. DDM-solubilized supernatants were loaded onto a TSKgel G4000SWxl column (Tosoh Bioscience) attached to a Prominence UFLC (Shimadzu) coupled to a RF-10AXL fluorescence detector (Shimadzu). These studies identified the PfCRT 7G8 construct as having the best yield and mono-dispersity.

PfCRT 7G8 protein expression, purification and reconstitution into nanodiscs

The *pfcrt* 7G8 full-length open reading frame was cloned into the pEG BacMam vector[33] using the Gibson Assembly method[34]. *pfcrt* was fused at its 3' end with a Tobacco Etch Virus (TEV) protease cleave site (ENLYFQSYV) and a decahistidine affinity tag followed by a streptavidin affinity tag (WSHPQFEK). The resulting plasmid was transformed into *Escherichia coli* DH10Bac competent cells to generate the bacmid using a bac-to-bac (Invitrogen) protocol. Recombinant P1 baculovirus was transfected into Sf9 cells (Expression System) in the presence of PEI and cultured in ESF 921 protein-free insect cell culture medium (Expression Systems). For protein expression, 100 ml P4 virus was used to infect 1-liter cultures of HEK293S GnTi$^-$ cells (Invitrogen) at 3×10^6 cells/ml in Freestyle 293 media (GIBCO) supplemented with 2% FBS (GIBCO). After infection, the cells were incubated at 37°C for 8 to 10 h in the presence of 8% CO_2 and 70% humidity. We then added 10 mM sodium butyrate (Sigma-Aldrich) to enhance BacMam protein expression. Cells were further incubated at 37°C for 48 h prior to harvest. Cell pellets were homogenized in low-salt buffer (10 mM HEPES pH 7.5, 10 mM KCl, 10 mM $MgCl_2$, 0.5 mM PMSF, cOmplete™ EDTA-free Protease Inhibitor Cocktail, 10 μg/ml DNase I, and 8 μg/ml RNase) in a glass homogenizer. Membrane fractions were isolated by ultracentrifugation at 40,000×*g* in a Type 45 Ti Rotor (Beckman Coulter). Membrane fractions were further homogenized and washed twice with high-salt buffer (10 mM HEPES pH 7.5, 10 mM KCl, 10 mM $MgCl_2$, 1 M NaCl, 0.5 mM PMSF, cOmplete Protease Inhibitor Cocktail, 10 μg/ml DNase I, and 8 μg/ml RNase) in a glass homogenizer followed by ultracentrifugation. The washed membrane fractions were resuspended again by homogenizing in buffer comprised of 20 mM HEPES pH 7.5, 200 mM NaCl and 0.5 mM PMSF, and cOmplete Protease Inhibitor Cocktail, and stored at −80°C until use.

The thawed membrane fraction was solubilized by adding DDM with CHS in a 10:1 (w/w) ratio to a final concentration of 1% (w/v) detergent, as per[35], and incubated at 4°C for 2 h with gentle agitation. Insoluble material was removed by ultracentrifugation at 40,000×*g* in a type 45 Ti rotor (Beckman Coulter) at 4°C for 30 min. The supernatant was filtered (0.22 μm filters, Millipore), placed in a Falcon tube containing pre-equilibrated Ni^{2+}-NTA resin (Qiagen) in the presence of 20 mM imidazole, and incubated at 4°C overnight with gentle rotation. The resin was washed with 10 column volumes of buffer comprising 20 mM HEPES pH 7.5, 200 mM NaCl, 60 mM imidazole, 0.1% DDM and 0.01% CHS. Bound protein was eluted with buffer consisting of 20 mM HEPES pH 7.5, 200 mM NaCl, 200 mM imidazole, 0.05% DDM and 0.005% CHS. The eluted protein was incorporated into lipid nanodiscs with a 1:400:10 molar ratio of protein:1-palmitoyl-2-oleoyl-sn-glycero-3-phospho-(1'-rac-glycerol) (POPG): membrane scaffold protein 1D1 (MSP1D1). This mixture was incubated at 4°C for 2.5 h with gentle agitation. Reconstitution was initiated by removing detergent by incubating with Bio-beads (Bio-Rad) at 4°C overnight with constant rotation. Bio-beads were removed and the nanodisc reconstitution mixture was bound again to Ni^{2+}-NTA resin for at 4°C for 2 h to remove free nanodiscs. The resin was washed with 10 column volumes of wash buffer (20 mM HEPES pH 7.5, 200 mM NaCl, and 20 mM Imidazole) followed by 4 column volumes of elution buffer (20 mM HEPES pH 7.5, 200 mM NaCl, and 200 mM Imidazole). The eluted protein was further purified by loading on a

Superdex 200 Increase 10/300 GL size-exclusion column (GE Healthcare Life Sciences) in gel filtration buffer (20 mM HEPES pH 7.0 and 150 mM NaCl).

Identification of PfCRT-specific Fab fragments using phage display

For the Fab screen, PfCRT 7G8 was reconstituted into nanodiscs using biotinylated MSP1D1. Prior to nanodisc assembly, MSP1D1 was chemically biotinylated as previously described[18,36,37]. Efficient biotinylation was confirmed using a pull-down assay with streptavidin-coated paramagnetic particles (Promega). Biopanning was performed using the Fab Library E[38,39] that expresses a subset of Fab fragments on the phage surface. Binding was assayed in Selection Buffer (25 mM HEPES pH 7.4, 150 mM NaCl, and 1% Bovine Serum Albumin). In the first round, biopanning was performed manually using 200 nM of PfCRT 7G8-MSP1D1 nanodiscs immobilized onto magnetic beads. Following three washes with Selection Buffer, the resuspended beads enriched for phage expressing PfCRT-specific Fab fragments were used to infect log-phase *E. coli* XL-1 Blue bacteria. Phages were amplified overnight in 2xYT media supplemented with ampicillin (100 μg/ml) and M13-KO7 helper phage (10^9 pfu/ml). To increase the stringency of selection, four additional rounds of biopanning were performed with decreasing target concentrations, from 150 nM to 75 nM to 40 nM to 20 nM. For each round, the amplified phage pool from each preceding round was used as the input. For rounds 2–5, biopanning was performed semi-automatically using a Kingfisher magnetic beads handler (Thermo Fisher Scientific). To reduce the presence of non-specific binders, the phage pool for rounds 2–5 was pre-cleared with 100 μl of streptavidin particles. For all rounds we used empty, non-biotinylated 1D1 nanodiscs as soluble competitors in excess, at a constant concentration of 1.5 μM. In rounds 2–5, bound phage particles were removed by elution from magnetic beads following a 15 min incubation step with 1% Fos-choline-12 prepared in Selection Buffer.

Single-point phage ELISA to validate Fab binding to PfCRT

The initial validation for selection was performed by single-point phage ELISA using individual clones from rounds 4 and 5. All ELISA experiments were performed in 96-well plates (Nunc) coated with 2 μg/ml Neutravidin and blocked with Selection Buffer. Colonies of *E. coli* XL1-Blue bacteria harboring phagemids were used to inoculate 400 μl 2xYT media supplemented with 100 μg/ml ampicillin and 10^9 pfu/ml M13-KO7 helper phage. Phages were amplified overnight in 96-well deep-well blocks at 37°C with shaking at 280 rpm. Amplified phages were diluted 10-fold into Selection Buffer and assayed against either PfCRT-loaded or empty biotinylated nanodiscs. Target proteins were immobilized at room temperature for 30 min followed by incubation with phage dilutions for 30 min. Bound phage particles were detected with TMB substrate (Thermo Fisher Scientific) following a 30 min incubation with horseradish peroxidase (HRP)-conjugated anti-M13 monoclonal antibody (GE Healthcare). The reaction was quenched with 1.0 M HCl and the absorbance was measured at 450 nm. Wells containing empty nanodiscs were used to determine non-specific binding.

Fab expression and purification

Specific binders from phage ELISA were selected based on their signal/background ratio[18] and were sequenced at the University of Chicago Comprehensive Cancer Center DNA

Sequencing facility. Unique clones were sub-cloned in pRH2.2 using the In-Fusion Cloning kit (Takara Bio). Sequence-verified Fab expression vectors were then transformed into *E. coli* BL21-Gold competent cells (Agilent), which were used to inoculate overnight cultures. Inocula were harvested the following morning to seed 1-liter 2xYT broth supplemented with 100 μg/ml ampicillin. Cultures were grown to an OD_{600} of 0.8 and then induced for 4 h at 37°C. Cells were harvested by centrifugation and stored at −80°C until use. Cell pellets were resuspended in buffer (20 mM HEPES pH 7.4, 150 mM NaCl, and 0.5 mM $MgCl_2$) supplemented with 1 mM PMSF and 1 μg/ml DNase I (Gold Biosciences). These preparations were sonicated (Branson Sonifier) until complete lysis was achieved. Lysates were incubated at 60°C for 30 min to eliminate potential Fab proteolysed fragments, subsequently cooled on ice, and cleared by centrifugation. Supernatants were filtered and then loaded onto a 5 ml HiTrap MabSelect SuRe column (GE Healthcare) equilibrated with Wash Buffer (20 mM HEPES pH 7.4 and 500 mM NaCl). The column was washed 10 times with Wash Buffer and Fabs were eluted with 0.1 M acetic acid. Fractions containing Fab fragments were loaded onto a 1 ml Resource S column (GE Healthcare) equilibrated with buffer A (50 mM sodium acetate, pH 5.0). Following washing with 10 column volumes of buffer A, Fab fragments were eluted by a linear 0–50% gradient with buffer B (50 mM sodium acetate, pH 5.0 and 2 M NaCl). Fractions containing Fab fragments were evaluated for purity by SDS-PAGE and subsequently pooled and dialyzed overnight in 20 mM HEPES pH 7.4 and 150 mM NaCl.

Assessment of Fab binding affinity for PfCRT

To estimate apparent binding affinity, we performed multi-point ELISA with purified Fab fragments[18], which were diluted serially 3-fold starting from a 3 μM maximum concentration. ELISA plates were coated and blocked as described above for the phage ELISA studies. 50 nM of biotinylated PfCRT 7G8-MSP1D1 nanodiscs were immobilized on the plates by 30 min incubation, followed by washing. Fab dilutions were added to wells containing immobilized PfCRT and allowed to bind for 30 min. Bound Fab was detected with TMB substrate following a 30 min incubation with HRP-conjugated mouse anti-human IgG $F(ab')_2$ monoclonal antibody (Jackson). Reactions were quenched with 1.0 M HCl and the absorbance was measured at 450 nm. A_{450} values were plotted against the $\log_{10}$ of the Fab concentration. EC_{50} values were then calculated in GraphPad Prism 8 using a variable slope model and assuming a sigmoidal dose response.

PfCRT 7G8 complex formation with the Fab CTC

Size-exclusion chromatography fractions of purified PfCRT in nanodiscs were incubated with the CTC Fab on ice for 2 h in a 1:3 molar ratio of protein to Fab. The PfCRT-Fab complex was then concentrated and filtered, and then loaded on a Superdex 200 Increase 10/300 GL size-exclusion column in gel filtration buffer (20 mM HEPES pH 7.0 and 150 mM NaCl).

Negative stain electron microscopy

To determine the sample quality and success of the Fab binding, purified protein was diluted to 0.01 mg/ml (for PfCRT without Fab) or 0.005 mg/ml (for PfCRT with Fab) and applied onto copper grids (Ted Pella). These grids were overlaid by a thin (~1.5 nm) layer of

continuous carbon that had been plasma-cleaned (Gatan Solarus) for 30 s using a mixture of H_2 and O_2. Thereafter, filter paper (Whatman 4) was used to remove the protein solution. 3 μl of 2% uranyl formate was then added and immediately removed by absorbing with filter paper – this was repeated seven times. The grid was imaged on either a Tecnai T12 microscope (FEI) (for PfCRT without Fab) or a Tecnai TF20 microscope (FEI) (for PfCRT with Fab). Both microscopes were equipped with a Tietz F416 CCD camera (Tietz) at 1.23 Å or 1.10 Å per pixel respectively, using the Leginon software package[40]. 166 and 87 images were collected respectively and were processed using the Appion software package[41] to obtain 2D classes with Relion 2.1[42,43]. The micrographs showed good particle dispersion. 2D class averages showed that the Fab addition resulted in a clear fiducial for particle alignment (Extended Data Fig. 2).

Single-particle cryo-EM vitrification and data acquisition

Purified PfCRT-Fab complex was concentrated to 1.56 mg/ml using a 30-kDa concentrator (Amicon). 2.5 μl of sample was added to a plasma-cleaned (Gatan Solarus) 1.2/1.3 μm holey gold grid (Quantifoil UltrAuFoil) and blotted using filter paper on one side for 2 s using the Leica GP plunger system, before plunging immediately into liquid ethane for vitrification. The plunger was operating at 6°C with >80% humidity to minimize evaporation and sample degradation. Images were recorded on a Titan Krios electron microscope (FEI) equipped with a C_s corrector and K2 summit direct detector (Gatan) operating at 0.5175 Å per pixel (calibrated using an AAV2 dataset) in counting mode using the Leginon software package[40]. An energy filter slit width of 20 eV was used during the collection and was aligned automatically every hour using Leginon. Data collection was performed using a dose of ~91.56 $e^-/Å^2$ across 80 frames (75 ms per frame) at a dose rate of ~4.0 e^-/pix/s, using a set defocus range of −1.2 μm to −1.8 μm. A 100 μm objective aperture was used. In total, 3,377 micrographs were recorded over a single 2.5-day collection using an image beam shift data collection strategy[44]. Ice thickness was monitored after every 4th exposure using the Leginon zero-loss peak (ZLP) algorithm[45] and was determined to be 23.1 ± 9.1 nm (SD).

Data processing

Movie frames were aligned using MotionCor2[46] with 3 by 3 patches, a grouping of 3, and a B-factor of 100, using the Appion software package[41]. Micrograph Contrast Transfer Function (CTF) estimations were performed using both CTFFind4[47] and GCTF[48], and the best estimates based on confidence were selected using the Appion software package. Micrographs that had estimated resolution at 0.5 confidence level of worse than 10 Å were removed, resulting in 3,297 micrographs. DoG picker[49] was used to pick 682,520 particles (extracted binned by 2), which were transferred into Relion 2.1[42,43] for 2D classification. 2D class averages that showed clear structural details of PfCRT were used as templates for template-based picking using Gautomatch (https://www.mrc-lmb.cam.ac.uk/kzhang/Gautomatch). To avoid missing any particles, we chose a lenient threshold that resulted in 1,095,304 initial picks. These were pared down to 183,241 particles after Relion 2D classification. Two rounds of CryoSPARC 2[50] *ab initio* (using 2 models) were then performed to further refine the particle stack to 35,682 particles, which yielded an 8.27 Å resolution upon 3D homogeneous refinement. Particles were then re-centred and re-extracted using Relion and per-particle CTF estimation using GCTF was then performed. The particle

stack was brought back into CryoSPARC for one round of *ab initio* refinement (using two models). The best set of particles and model was then used for non-uniform refinement. This resulted in a 3.7 Å map from 17,034 particles.

The mag_distortion_correct software[51] was then used on the micrographs to correct for magnification anisotropy of 1.3%, which was determined previously using gold-replica grating using the mag_distortion_estimate software[51]. The resulting particles were then subjected to three rounds of CryoSPARC non-uniform refinement, re-centering and re-extracting in Relion, with removal of overlapped particles centered no more than 20 pixels from each other, and CTF refinement using *cis*TEM[52]. This resulted in a 3.6 Å density map from 17,030 particles.

To optimize the alignment of frames, movie frames were re-aligned using MotionCor2 with 2 by 2 patches, a grouping of 3, correction for in-frame motion, and a B-factor of 150 for global frame alignment and 50 for local frame alignment. Visual inspection of the resulting micrographs showed that certain micrographs fared better using the new frame alignment parameters, while some fared worse than with the 3 by 3 patches described above. To determine the best frame alignment parameter on a per-particle basis, particles were extracted from micrographs using both conditions. These particles were then subjected to a CryoSPARC 2 non-uniform refinement and one round of *cis*TEM refinement. Thereafter, we chose the alignment parameter that produced the highest score. This resulted in 7,191 particles coming from micrographs aligned with 2 by 2 patches, and 9,714 particles coming from micrographs aligned with 3 by 3 patches. Particle polishing algorithms that require neighboring particles to aid in alignment were tested but gave consistently worse results, likely because of the low average number of particles per micrograph (~5.3) caused by the high magnification used and sizeable number of free Fab contaminants.

Thereafter, signal subtraction using Relion was performed. Subtraction of just the nanodisc did not improve the overall resolution. However, subtraction of both the nanodisc and constant domain of the Fab improved the resolution of the reconstruction, after CryoSPARC non-uniform refinement, to 3.3 Å overall, and 3.2 Å for PfCRT alone. This final map was sharpened using phenix.auto_sharpen[53], which automatically selected b_iso sharpening to high_resolution cutoff as the algorithm to use. Overall b_sharpen applied was 28.3 $Å^2$, final b_iso obtained was 47.3 $Å^2$ and the high-resolution cut-off was 3.2 Å. All conversions between Relion, CryoSPARC, and *cis*TEM were performed using Daniel Asarnow's pyem script (unpublished, https://github.com/asarnow/pyem).

Structural model building and refinement

To build the PfCRT model, we first used the Chimera[54] program to approximately segment out the PfCRT part of the map from the nanodisc and Fab density. *De novo* model building for the PfCRT primary sequence in the cryo-EM map was initiated using Rosetta[55]. After two rounds of Rosetta model building, the partial model was brought into Coot[56] for manual model building. For Fab model building, the Fab portion of the deposited yeast nucleoprotein complex (PDB-ID:4XMM[57]) was used as a starting template, as it had the same scaffold backbone. An extra electron density between PfCRT helices 1, 9 and 10 was not modelled by protein density and was likely of lipid origin. Out of the lipids present in

the nanodisc, CHS produced the best density fit and was therefore incorporated into the model.

Thereafter, model adjustment and refinement were performed iteratively in Coot and Phenix, with the statistics examined using Molprobity[58] until no further improvements were observed. The final map and model were then validated using: 1) EMRinger[59] to compare map to model; 2) ResMap[60] to calculate map local resolution; and 3) a program suite with 3D Fourier shell correlations (FSC)[61]. To calculate the FSC values, we used a cut-off criterion of 0.143[62]. The 3D FSC program suite[61] was used to calculate the degree of directional resolution anisotropy. Map-to-model FSCs were also calculated by first converting the model to a map using the Chimera molmap function at Nyquist resolution (2.07 Å). A mask was generated from this map using Relion (after low-pass filtering to 8 Å, extending by 1 pixel and applying a cosine-edge of 3 pixels), and was then applied to the density map. Map-to-model FSC was calculated using EMAN[63].

Model analysis

A cavity search using the Solvent Extractor from Voss Volume Voxelator server[64] was performed using an outer probe radius of 10 Å and inner probe radius of 3 Å. We then used a Dali server[65] to search for other PDB structures with a similar fold. This search produced top results for Vrg4 (PDB ID: 5OGE/5OGK)[66], YddG (PDB ID: 5I20)[67], TPT (PDB ID: 5Y78/5Y79)[68], zmCST (PDB ID: 6I1R)[69] and mCST (PDB ID: 6OH4)[70], with Z scores from 26.7 to 16.0. Thereafter, there was a large drop in Z score for the next best hit at 8.5 (the chloride pumping rhodopsin, PDB ID: 5B2N) that visually did not superimpose well with PfCRT (Root mean square deviation of superimposition was 8.1 Å).

Amino acid sequence alignments

For conservation analysis in Apicomplexan parasites, we obtained 11 orthologs of CRT from OrthoMCL-DB[71]. Their amino acid sequences, in addition to the PfCRT isoforms Dd2 and WT, were then aligned using MUSCLE[72], resulting in 13 orthologs in total. For the sequences used for Extended Data Fig. 7, the sequences used are *Plasmodium falciparum* PfCRT strain 7G8 (UNIPROT W7FI62) and its orthologs PfCRT Dd2 (UNIPROT F5CEB4), PfCRT-WT (the canonical 3D7 wild-type sequence; UNIPROT Q9N623), *P. reichenowi* CRT (PrCRT; UNIPROT A0A2P9D9K2), *P. vivax* CRT strain Sal-1 (PvCRT; UNIPROT Q9GSD3), *P. knowlesi* CRT strain H (PkCRT; UNIPROT Q9GSD7), *P. berghei* CRT strain ANKA (PbCRT; UNIPROT Q9GSD8), *P. chabaudi* CRT strain chabaudi (PcCRT; UNIPROT Q7Z0V9), *Babesia microti* CRT strain RI (BmCRT; UNIPROT A0A1N6LY67), *Theileria annulata* CRT strain Ankara (TaCRT, UNIPROT Q4UDS9); *Eimeria tenella* CRT (EtCRT; UNIPROT U6L1M8), *Toxoplasma gondii* CRT (TgCRT; UNIPROT S8EU26), and *Cryptosporidium hominis* CRT strain TU502 (ChCRT; UNIPROT A0A0S4THJ3). Multiple sequence alignments were displayed using ESPript[73].

Computational studies

All calculations were performed using the Schrödinger molecular modeling suite (version 2019–1). The PfCRT protein structure solved herein was analyzed using the Protein Preparation Wizard[74]. In this step, force field atom types and bond orders were assigned,

missing atoms including hydrogens were added, tautomer/ionization states were assigned, Asn, Gln and His residues were flipped to optimize the hydrogen bond network, and a constrained energy minimization was performed. For mutation modeling, single point mutations were introduced into the PfCRT 7G8 structure using the Residue and Loop Mutation tool. The refinement step consisted of a local minimization in implicit solvent with Prime[75].

For molecular dynamics simulations, we employed the same protocol to simulate the 7G8 isoform and the different single amino acid variants. First, the protein was aligned so that the membrane plane corresponded to the xy plane of the coordinate system, using the OPM (Orientation of Proteins in Membranes) database[76]. Then, the protein was embedded in a POPC membrane model, included in an orthorhombic box of SPC water solvent with a 10 Å buffer on each dimension, and neutralized by adding appropriate number of Cl^- ions, using the System Builder panel. The molecular dynamics simulations were performed using Desmond[77]. Each simulation started with a system relaxation with a default protocol that was followed by a 250ns production run in an NPgT ensemble, at a temperature of 300K and a pressure of 1.01325 Bar. The resulting trajectories were analyzed using the Simulation Event Analysis tool to monitor distances of interest and the frames for each trajectory were clustered using the Desmond Trajectory tool.

The Poisson-Boltzmann ESP panel, which uses the Adaptive Poisson-Boltzmann Solver (APBS) method, was used to calculate the electrostatic surface potentials. The solute and solvent dielectric constants were set to 1 and 80 respectively, solvent radius was 1.4 Å, temperature was 298K and grid extension was 5 Å. The open-to-cytosol homology model of PfCRT was created using Maestro's Multiple Sequence Alignment tool. Leveraging PfCRT's inverted structural repeats that are related by two-fold pseudo-symmetry, the sequence of each TM helix was aligned and mapped onto the structure of the related TM helix, as previously carried out for other transporters with inverted structural repeats[67,78–80]. The positions of the loops and JM helices in the open-to-cytosol conformation could not be defined owing to a lack of homology in these regions. The individually aligned TM helices were merged to give the final model, which was further refined using restrained minimization from the Protein Preparation Wizard panel[74].

Production of *pfcrt* gene-edited parasites

7G8 parasites were engineered to express *pfcrt* variants that added the F145I or C350R mutations, or the 7G8 reference sequence, into the 7G8 coding sequence, using a previously published method based on zinc-finger nuclease-mediated gene editing[9,81]. Edited clones were recovered by limiting dilution.

[^{3}H]-CQ and [^{3}H]-PPQ accumulation assays in cultured parasites

This protocol has been previously described in detail[82]. Briefly, sorbitol-synchronized parasite cultures of recombinant 7G8, 7G8+F145I, 7G8+C350R, Dd2, and 3D7 (expressing WT *pfcrt*) were harvested as early trophozoites (24–26 h post-invasion) and magnet-purified (VarioMACS, Miltenyi Biotec). These lines are referred to herein as 7G8, 7G8+F145I, 7G8+C350R, Dd2 and WT (3D7). The pure trophozoite-infected erythrocytes were eluted in

fresh 1×PBS (37°C) containing 2 mM EDTA and supplemented with 0.5% BSA. The eluate was then centrifuged (1,500×rpm, 5 min), and the pellet washed and resuspended in bicarbonate-free RPMI 1640 medium (supplemented with 25 mM HEPES, 10 mM glucose, and 0.2 mM hypoxanthine, and adjusted to pH 7.4 at 37°C). The exact incubation cell numbers were determined by counting an aliquot of the resuspended cells using a hemocytometer counter. Uptake measurements began with the addition of 250 µl of trophozoite suspension, at an estimated hematocrit of 30,000–120,000 cells/µl, to an equal volume of 10 nM [^{3}H]-CQ (5.2 Ci/mmol; American Radiolabeled Chemicals) or 40 nM [^{3}H]-PPQ (15 Ci/mmol; American Radiolabeled Chemicals) in bicarbonate-free media to yield final [^{3}H]-CQ and [^{3}H]-PPQ concentrations of 5 nM and 20 nM, respectively. Parallel control measurements were conducted with uninfected erythrocytes at the same hematocrit. After 1 h of incubation at 37°C in a water bath, duplicate 200 µl aliquots of the suspensions were transferred into 1.5 ml Eppendorf tubes containing 300 µl of dibutyl phthalate (Sigma Aldrich, 1.04 g/ml) and centrifuged immediately (13,000×rpm; 2 min) to sediment the cells through the oil, thereby terminating [^{3}H]-drug uptake. From each duplicate, 100 µl of supernatant was transferred into a vial containing 5 ml of scintillation fluid (CytoScint™, MP Biomedicals) to determine the external drug concentration [Drug $_{external}$]. The pellets were digested by overnight incubation at 55°C with 100 µl tissue solubilizer (NCS-II, GE Healthcare) diluted 1:2 in absolute ethanol, then bleached the next day with 30% hydrogen peroxide (25 µl) followed by addition of 25 µl glacial acetic acid to block luminescence. Digested pellets were transferred into a vial containing 10 ml of scintillation cocktail and measured in a scintillation counter to determine the internal drug concentration [Drug $_{internal}$]. After adjusting for non-specific uptake by subtracting measurements from the uninfected erythrocyte controls, intracellular accumulation ratio was calculated as the ratio of [Drug $_{internal}$] / [Drug $_{external}$], normalized to 1×10^6 infected erythrocytes and assuming a mean volume of a trophozoite-infected erythrocyte of 75 fl[83].

Parasite piperaquine survival assays

PPQ survival assays were carried out as previously described with slight modifications[84]. Briefly, double sorbitol synchronized ring-stage parasites (0–6 h post invasion) were seeded at 1% parasitemia and 1% hematocrit in 96-well flat bottom plates containing a 2-fold, 8-point PPQ drug dilutions starting at 1600 nM. Parasites were incubated with the drug for 48 h at 37°C. Drug was then removed by washing the plates 4 times with complete media using a TECAN Freedom EVO 100 liquid handler. The assay plates were further incubated for 24 h before the parasitemias were measured using an Accuri C6 flow cytometer by double staining with SYBR Green I and MitoTracker Deep Red (to label DNA and the mitochondria, respectively). Percent survival was calculated for each line by dividing the parasitemia of the PPQ-treated parasites with the parasitemia of the no-drug control. Statistical significance was determined via nonparametric, two-tailed Mann-Whitney *U* tests using GraphPad Prism 8 software.

Parasite drug susceptibility assays

Parasite susceptibility to antimalarial drugs was measured by incubating asynchronous asexual blood-stage parasites to a range of drug concentrations (2-fold, 10 point) starting at 0.3% parasitemia and 1% hematocrit in 96-well plates. The assay plates were incubated at

37°C for 72 h in an environment with 5% O_2/5% CO_2/90% N_2. Final parasitemias were measured using flow cytometry. IC_{50} values were calculated by nonlinear regression analysis. Drug susceptibility assays were performed with chloroquine (CQ), monodesethyl-chloroquine (md-CQ, the *in vivo* metabolite of CQ), and piperaquine (PPQ). Statistical significance was determined via nonparametric, two-tailed Mann-Whitney *U* tests using GraphPad Prism 8 software.

Binding studies

All radiolabeled compounds were purchased from American Radiolabeled Chemicals. Unless other concentrations are indicated, binding experiments employed 125 nM [^{3}H]-Arg (40 Ci/mmol), 370 nM [^{3}H]-CQ (5.45 Ci/mmol), or 75 nM [^{3}H]-PPQ (15 Ci/mmol). Scintillation proximity assay (SPA)-based binding[20] of 200 ng of PfCRT 7G8, reconstituted into nanodiscs, was assayed in buffer composed of 50 mM Tris/Mes, pH 7.5, 5 % glycerol, 0.1 mM TCEP, 0.1 % PEI in the presence of 125 μg of YSi-His Tag SPA beads (Perkin Elmer), and in the presence or absence of indicated reagents or Fab. 800 mM imidazole, which competes with the His tag (fused to PfCRT) for binding to the copper-coated YSi SPA beads, was used to determine the non-proximity background signal. Concentrations of radiolabeled compounds were chosen in pilot experiments to obtain a signal-to-noise ratio ≥ 5, and specific binding was determined by subtracting the counts per minute in the presence of imidazole from the counts per minute measured in its absence. Control binding experiments of [^{3}H]-CQ employed nanodiscs containing 100 ng of the unrelated *Aquifex aeolicus* bacterial amino acid transporter LeuT. Since the SPA technology prevented reliable binding experiments at pH < 7.5, binding of [^{3}H]-CQ (1 Ci/mmol) or [^{3}H]-PPQ (2.5 Ci/mmol) was performed with equilibrium dialysis using the HTD96b dialysis 96-well apparatus and 12,000–14,000 MWCO membranes in 50 mM Tris/Mes, pH 7.5 or 5.5, 5 % glycerol, 0.1 mM TCEP for 4 h at 4ºC with 4.2 pmol of the indicated PfCRT variant in nanodiscs[85]. Non-linear regression analysis of the data was performed with GraphPad Prism 7. Kinetic constants represent the mean ± SEM of the fit.

Transport measurements

Purified PfCRT variants were reconstituted in preformed liposomes made of *E. coli* total lipids:CHS 94:6 (w/w) at a protein-to-lipid ratio of 1:150 (w/w). The lumen of the proteoliposomes was composed of 100 mM KP_i, pH 7.5 and 2 mM β-mercaptoethanol. Uptake of [^{3}H]-Arg (40 Ci/mmol), [^{3}H]-CQ (5.45 Ci/mmol), or [^{3}H]-PPQ (15 Ci/mmol) was performed by diluting PfCRT-containing proteoliposomes (40 ng PfCRT per assay) in 50 μl of 100 mM Tris/Mes, pH 5.5 in the presence or absence of indicated compounds. Unless indicated otherwise, 1 μM valinomycin (Vlm) was added to the reaction to generate a K^+ diffusion potential-driven membrane potential. The reactions were stopped after the indicated time periods by the addition of ice-cold 100 mM KP_i, pH 6.0/100 mM LiCl and filtered through 0.45 μm nitrocellulose filters (Millipore). Filters were dried and incubated in scintillation cocktail, and the radioactivity captured on the filters was counted in a Hidex SL300 scintillation counter. Specific radioactivity of all compounds was confirmed by counting known amounts of each radiolabel by determination of the decays-per-minute (dpm) to transform the dpm of the samples into pmol. Unspecific binding of all compounds with the nitrocellulose filters was determined by measuring mock uptakes in the absence of

liposomes or proteoliposomes, and these values (determined for each experiment) were used to calculate the uptake activity in liposomes or proteoliposomes. The specific uptake was determined by subtracting the time-dependent accumulation of the tested compounds in control liposomes (lacking PfCRT) from that measured in PfCRT-containing proteoliposomes. Kinetic constants (K_m and V_{max}) were determined by measuring the initial rates of [^{3}H]-Arg, [^{3}H]-CQ, or [^{3}H]-PPQ for periods of 3 s by fitting the data to the Michaelis-Menten equation in GraphPad Prism 7 and represent the mean ± SEM of the fit.

Extended Data

a

Haplotype	Region	Mutations	PfCRT haplotype											Drug phenotype	
			72	74	75	76	145	220	271	326	350	356	371	CQ	PPQ
3D7 (wild-type)	Africa	0	C	M	N	K	F	A	Q	N	C	I	R	S	S
7G8	S. America, W. Pacific	5	S	--	--	T	--	S	--	D	--	L	--	R	S
7G8+C350R	French Guiana (S. America)	6	S	--	--	T	--	S	--	D	R	L	--	S	R (low)
Dd2	SE Asia	8	--	I	E	T	--	S	E	S	--	T	I	R	S
Dd2+F145I	Cambodia	9	--	I	E	T	I	S	E	S	--	T	I	S[a]	R

Mutations in the reference Dd2 allele are shown in light grey. Other mutations are in dark grey. S, sensitive; R, resistant.

[a]Sensitized to CQ compared to parental line but not fully sensitive.

b

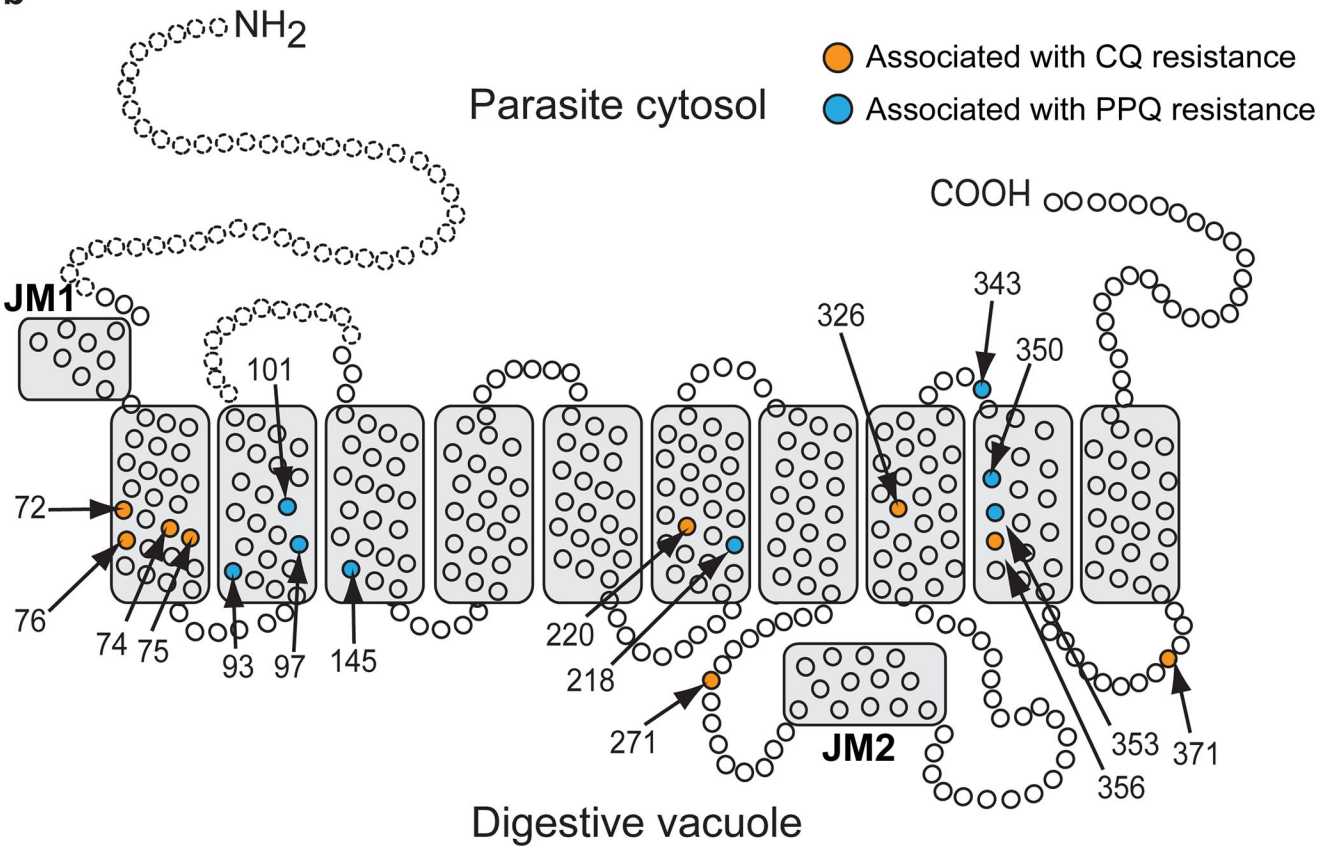

Extended Data Figure 1. Major PfCRT haplotypes and location of residues involved in chloroquine (CQ) or piperaquine (PPQ) drug resistance phenotypes.

a, Listing of the PfCRT canonical CQ-S, PPQ-S 3D7 haplotype, the CQ-R 7G8 (South America and Western Pacific) and Dd2 (Southeast Asia) haplotypes, and the 7G8+C350R and Dd2+F145I variants that have emerged in *P. falciparum* parasites in malaria-endemic areas and are associated with PPQ resistance. **b**, Localization of PfCRT mutations, based on the solved PfCRT structure. Most mutations localize within or near the boundary of one of the 10 TM helices. JM, juxtamembrane. Extended Data Table 2 provides additional information about PfCRT mutations observed in the field or obtained in drug-pressured cultured parasites.

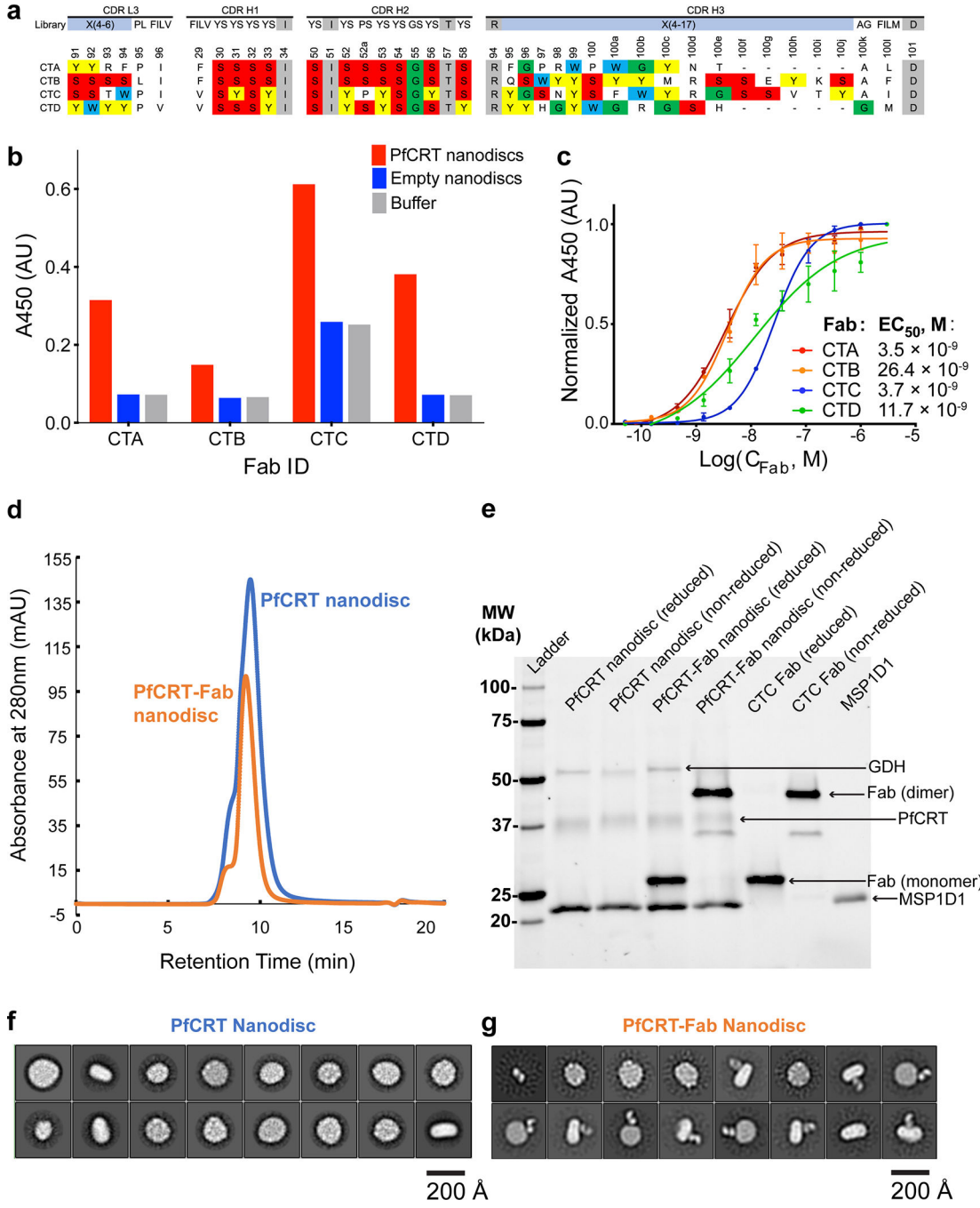

Extended Data Figure 2. Identification of PfCRT-specific antigen-binding fragments (Fab) and preparation of purified PfCRT ± Fab protein in nanodiscs.

a, Complementarity-determining region (CDR) sequences of unique antigen-binding fragments (Fabs) panned for binding to recombinant PfCRT 7G8 incorporated into MSP1D1 nanodiscs. Fabs were selected following multiple rounds of enrichment from the phage display library E[38,39,86]. Enriched SYGW residues are highlighted by color code (red, yellow, green and blue, respectively) and are numbered according to the Kabat system[87]. Tyr (Y), Ser (S), Gly (G), and Trp (W) residues, which play a dominant role in antigen

recognition, are shown in yellow, red, green, or blue, respectively, and are numbered according to the Kabat system[87]. CTC was selected to form a stable PfCRT 7G8-Fab complex. **b**, Single-point ELISA quantifying the binding of phage-displayed Fab to PfCRT-incorporated biotinylated nanodiscs, empty nanodiscs, or buffer (empty wells), measured at 450 nm absorbance (n=1). **c**, EC_{50} evaluation for purified Fab binding to PfCRT incorporated into biotinylated nanodiscs, showing high-affinity binding for the Fab CTC (3.7 nM). Data points show average values from independent experiments run in triplicate and error bars display the standard deviations from the means. **d**, High-performance liquid chromatography profile of PfCRT 7G8 ± bound Fab CTC. **e**, SDS-PAGE gel of pooled and concentrated size-exclusion chromatography fractions from PfCRT 7G8 ± Fab CTC. The contaminant glutamate dehydrogenase, GDH (present as a left shoulder in **d**), was excluded from single-particle analyses. MSP1D1 is a membrane scaffold protein used to assemble the nanodiscs. The identity of PfCRT and GDH was confirmed using mass spectrometry. **f**, Representative negative stain 2D class averages from Relion[42] 2D classification of nanodisc-incorporated PfCRT without Fab. **g**, Representative negative stain 2D class averages from Relion 2D classification of nanodisc-incorporated PfCRT with bound CTC Fab.

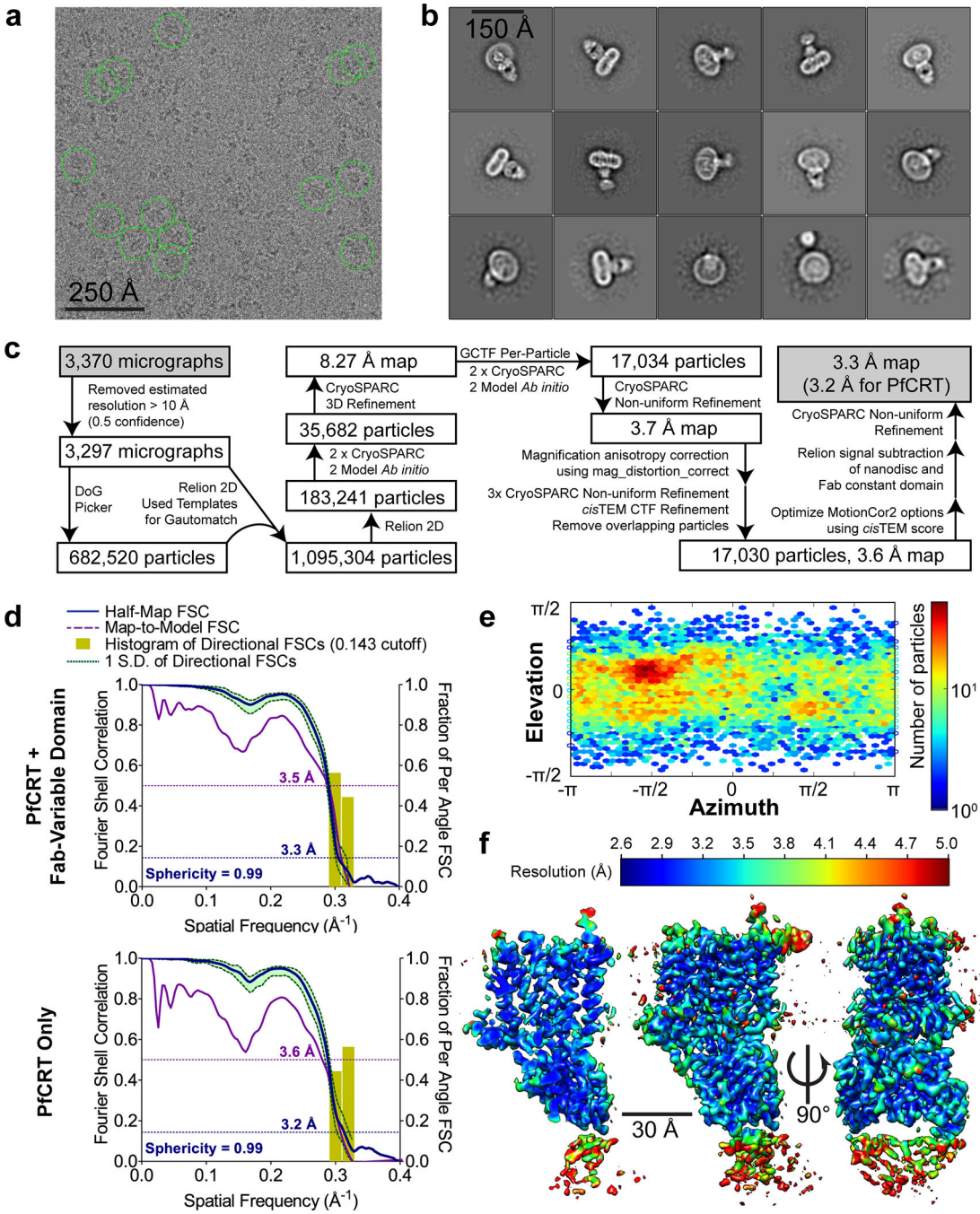

Extended Data Figure 3 |. Cryo-EM analysis of the PfCRT 7G8-Fab CTC complex.

a, Representative micrograph (0.5175 Å per pixel, 1.65 μm defocus). Exemplar picked particles contributing to the final reconstruction are circled in green. **b,** Representative 2D class averages from Relion 2D classification. **c**, Flowchart of cryo-EM data processing and refinement of the PfCRT 7G8-Fab CTC complex. See Methods for details. **d,** Fourier shell correlation (FSC) curves for PfCRT 7G8 complexed with the Fab CTC variable domain as well as for PfCRT alone. Data show the half-map (blue) and map-to-model (purple) resolutions (at 0.143 and 0.5 cut-offs respectively), with embedded histograms of directional

resolutions sampled evenly over the 3D-FSC[61] (yellow). The corresponding sphericity values are indicated. **e,** Euler angle distribution plot of the final 3D reconstruction from CryoSPARC 2[50]. **f,** Local resolution[88] display of unsharpened reconstructions of PfCRT complexed with the CTC Fab variable domain, in orthogonal views, sliced through the density for the first view.

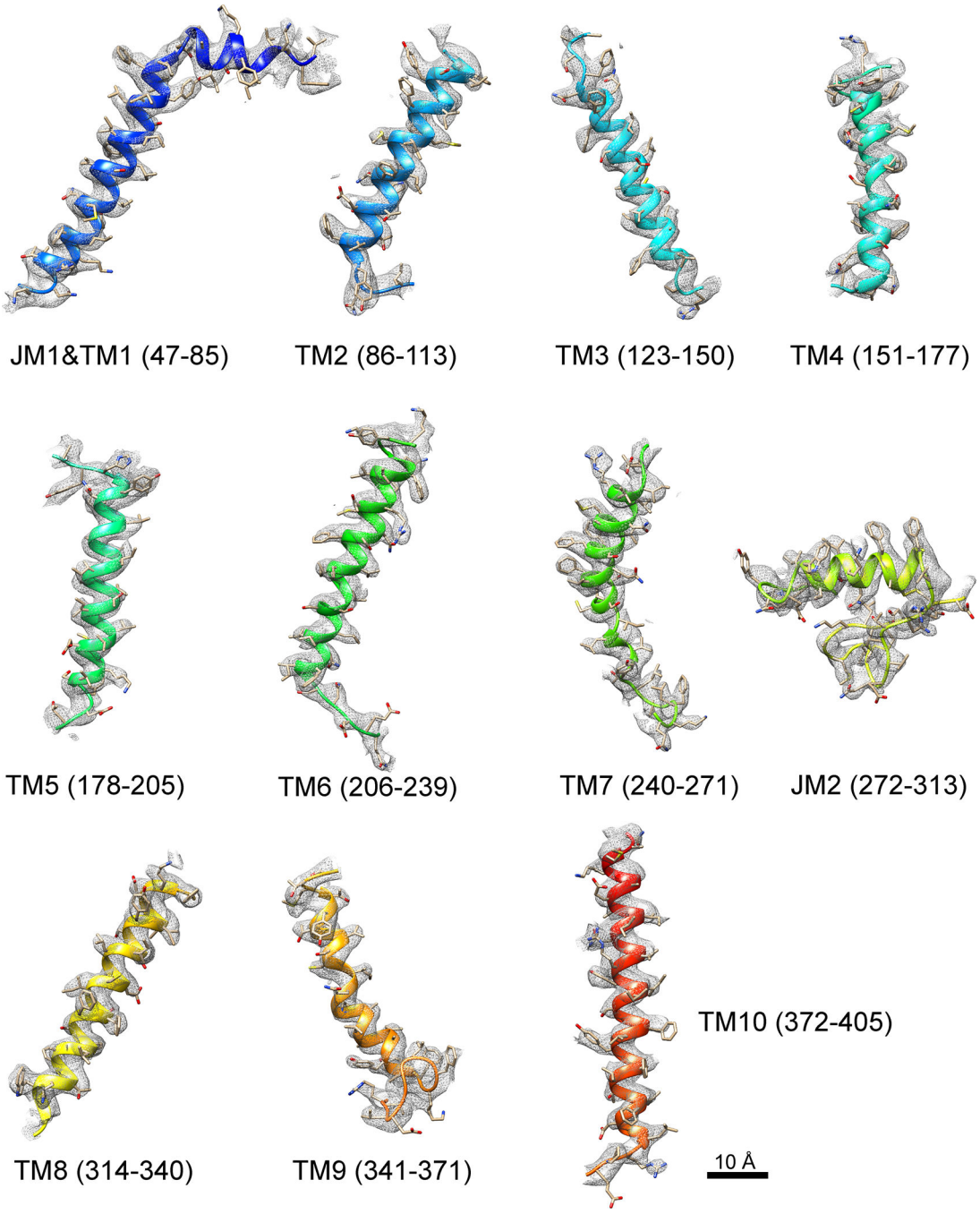

Extended Data Figure 4 |. Fit of cryo-EM density with model.

Cryo-EM densities (mesh) are superimposed with TM and JM helices of the PfCRT model. The model is rendered as a cartoon, colored in rainbow.

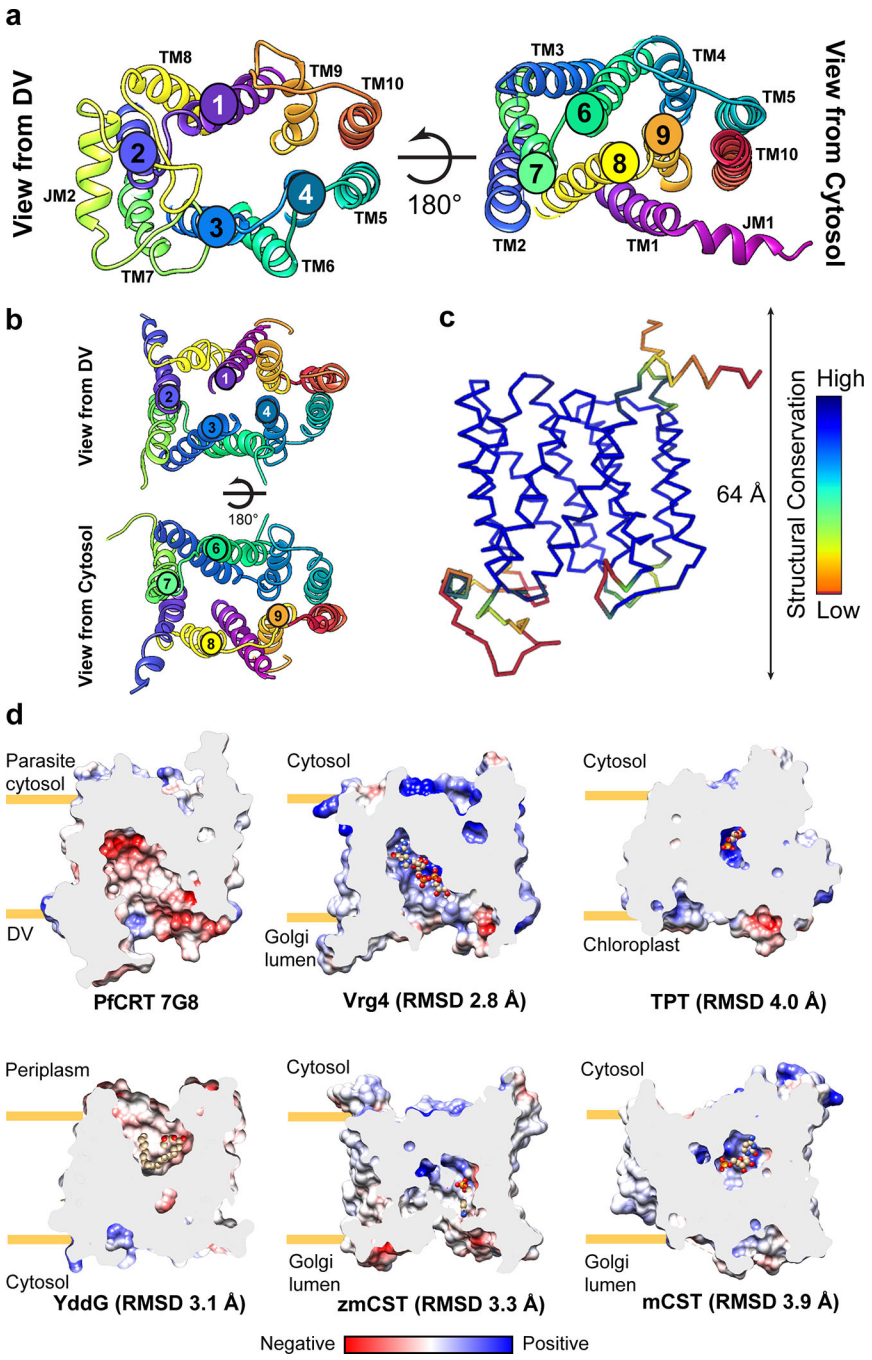

Extended Data Figure 5 |. PfCRT symmetrical arrangement, topology of TM helices, and structural comparison with other DMT superfamily members.

a, View of PfCRT from opposite directions of the DV and cytosol, with labeling of the four helices closest to the center (thus contributing to the cavity). **b**, Model of the TM helices in the PfCRT 7G8 structure in the open-to-cytosol conformation. **c**, Structural conservation of PfCRT compared with the DMT family members Vrg4 (a GDP-mannose transporter; PDB ID: 5OGE/5OGK)[66], YddG (an amino acid transporter; PDB ID: 5I20)[67], TPT (a triose-phosphate/phosphate translocator; PDB ID: 5Y78/5Y79)[68], and zmCST and mCST (two

CMP-sialic acid transporters; PDB IDs: 6I1R and 6OH4, respectively)[69,70]. Conservation profiles were generated using the Dali server[65]. **d**, Electrostatic representation of slices revealing the cavities of these six proteins in their solved structural states. Note the highly negatively charged (red) residues in the PfCRT cavity, contrasting with the positively charged (blue) or neutral residues in the other DMT transporters (shown as slices to emphasize the individual cavities). Ligands for the non-PfCRT transporters are shown in a ball and stick representation.

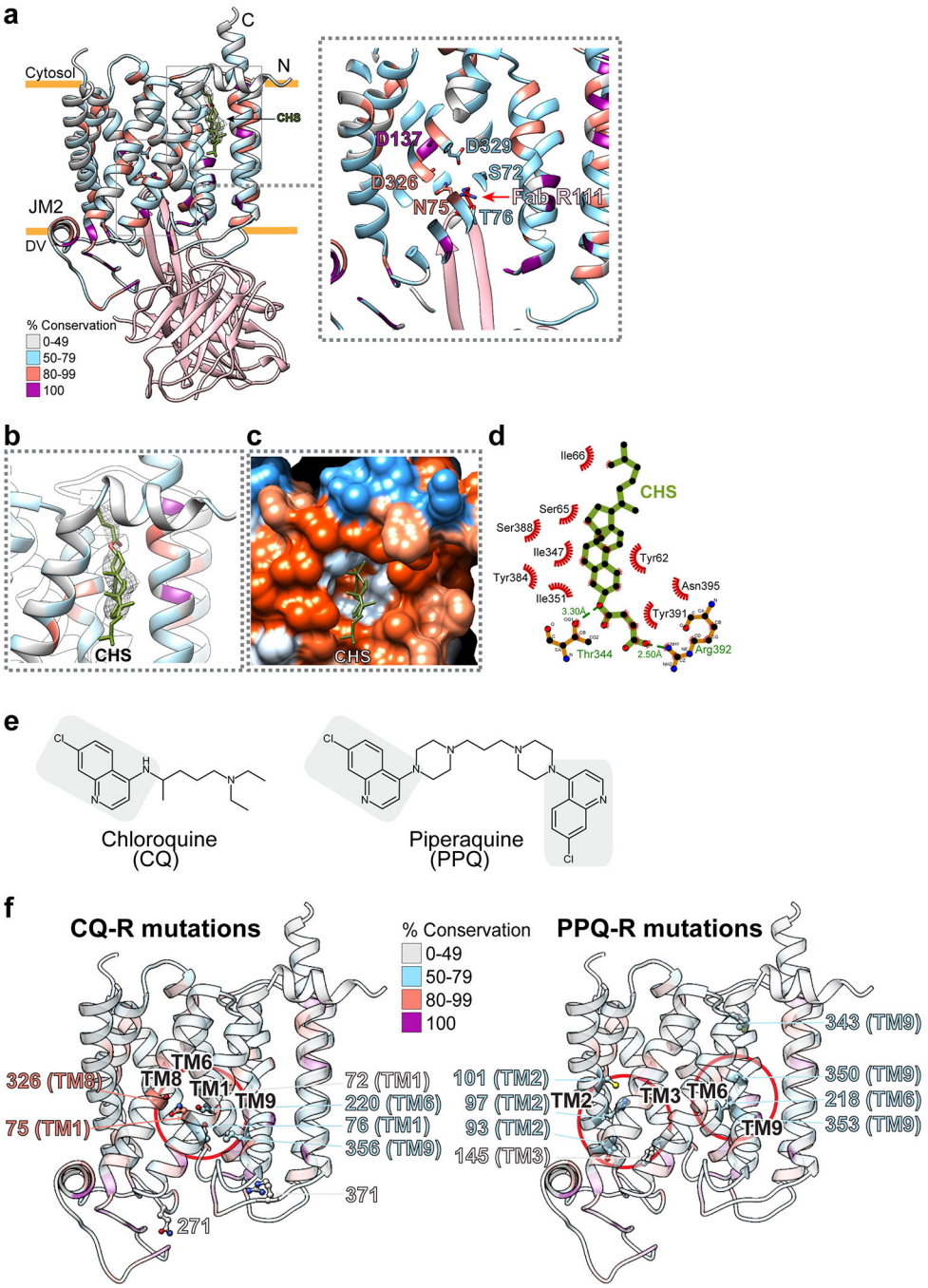

Extended Data Figure 6 |. Structure of the PfCRT 7G8-Fab CTC complex showing sequence conservation, localization of cholesteryl hemisuccinate (CHS), chemical structure of CQ and PPQ, and conservation of CQ-R and PPQ-R mutations.

a, PfCRT and the bound Fab are rendered in cartoon. PfCRT is colored according to sequence conservation (see Extended Data Fig. 7) and the Fab is colored in pink. Inset shows a magnified view of the interaction between PfCRT 7G8 and the Fab CTC. **b**, PfCRT cleft formed by JM1, TM1, TM9 and TM10 demonstrates CHS placement. **c**, PfCRT is rendered as a surface colored by hydrophobicity, from orange (hydrophobic) to blue (hydrophilic). **d**, 2D diagram of PfCRT-CHS interactions observed in the structure,

generated using LigPlot[+89]. **e**, Chemical structures of CQ and PPQ, with the 4-aminoquinoline rings shaded. **f**, Location of CQ (left) and PPQ (right) resistance-associated mutations (with side chains rendered as sticks and spheres), modeled onto the PfCRT 7G8 structure. Models are color coded according to sequence conservation derived from 11 Apicomplexan species (Extended Data Figure 7). TM helices associated with CQ or PPQ resistance are labeled and the areas highlighted with colored circles.

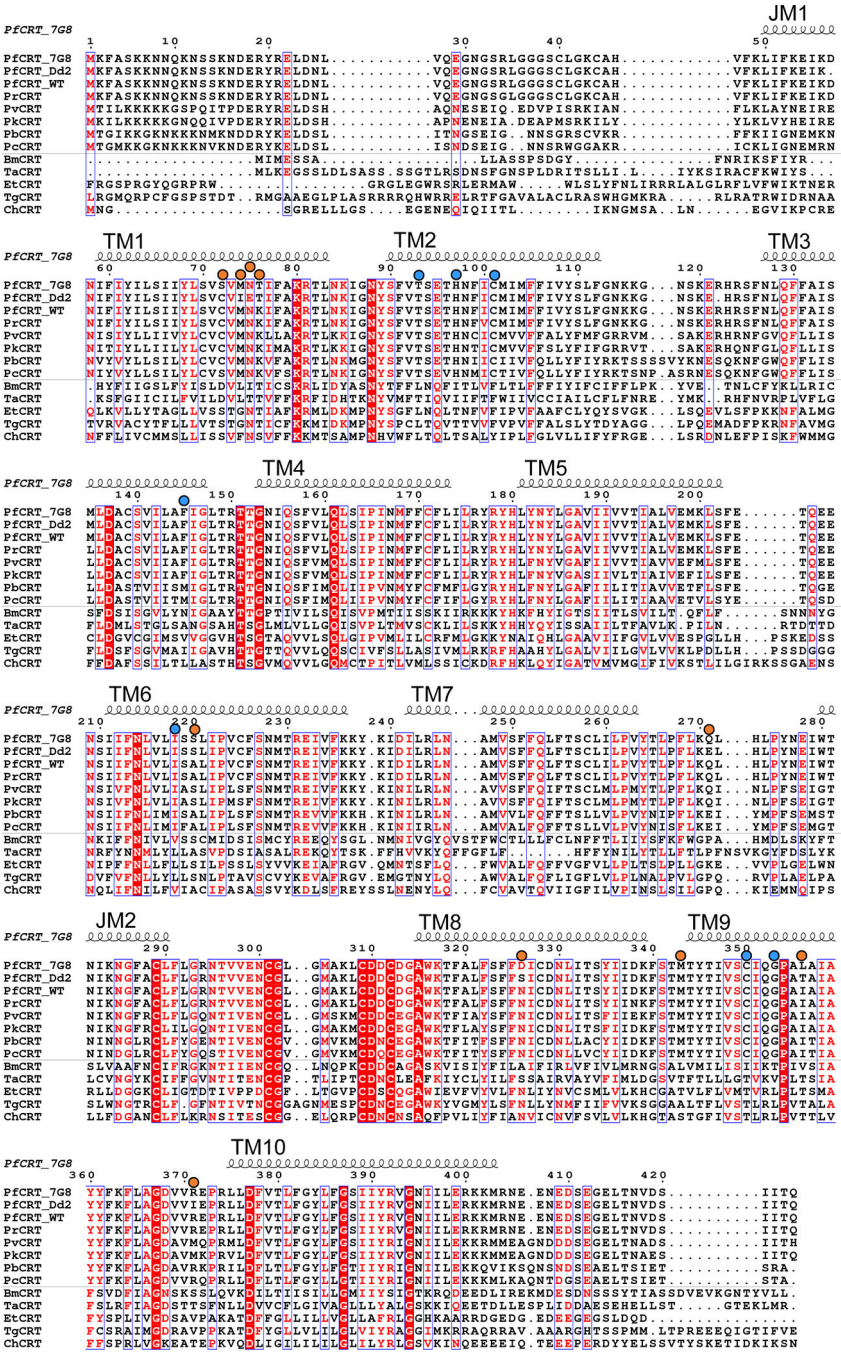

Extended Data Figure 7 |. Sequence alignment and secondary structure of PfCRT.
Sequences of different PfCRT isoforms and other CRT homologs were aligned using MUSCLE[72] and displayed using ESPript[73]. Sequences of nine orthologs of CRT in other *Plasmodium* or other Apicomplexan parasites were obtained from OrthoMCL-DB[71]. The sequences used are PfCRT 7G8 (UNIPROT W7FI62) and its orthologs PfCRT Dd2 (UNIPROT F5CEB4) and PfCRT WT (the canonical 3D7 wild-type sequence; UNIPROT Q9N623), *P. reichenowi* CRT (PrCRT; UNIPROT A0A2P9D9K2), *P. vivax* CRT strain Sal-1 (PvCRT; UNIPROT Q9GSD3), *P. knowlesi* CRT strain H (PkCRT; UNIPROT Q9GSD7), *P.*

berghei CRT strain ANKA (PbCRT; UNIPROT Q9GSD8), *P. chabaudi* CRT strain chabaudi (PcCRT; UNIPROT Q7Z0V9), *Babesia microti* CRT strain RI (BmCRT; UNIPROT A0A1N6LY67), *Theileria annulata* CRT strain Ankara (TaCRT, UNIPROT Q4UDS9); *Eimeria tenella* CRT (EtCRT; UNIPROT U6L1M8), *Toxoplasma gondii* CRT (TgCRT; UNIPROT S8EU26), and *Cryptosporidium hominis* CRT strain TU502 (ChCRT; UNIPROT A0A0S4THJ3). The secondary structure of PfCRT is shown as a cartoon above the alignments with residue numbering corresponding to the PfCRT 7G8 reference, along with the positioning of the variant residues indicated in Extended Data Fig. 1 (sharing the same color scheme). The highly-conserved cysteine residues that likely form disulfide bonds are C289-C312 and C301-C309. The degree of conservation was calculated by considering all sequences including *P. falciparum* 3D7 (WT) but excluding the 7G8 and Dd2 variants. Residues conserved (i.e. identical or similar) in at least 10 of 13 species are indicated in red text. Residues conserved in all species are in white text with red highlighting. None of the mutations associated with CQ or PPQ resistance mapped to residues that are fully conserved across these Apicomplexan species.

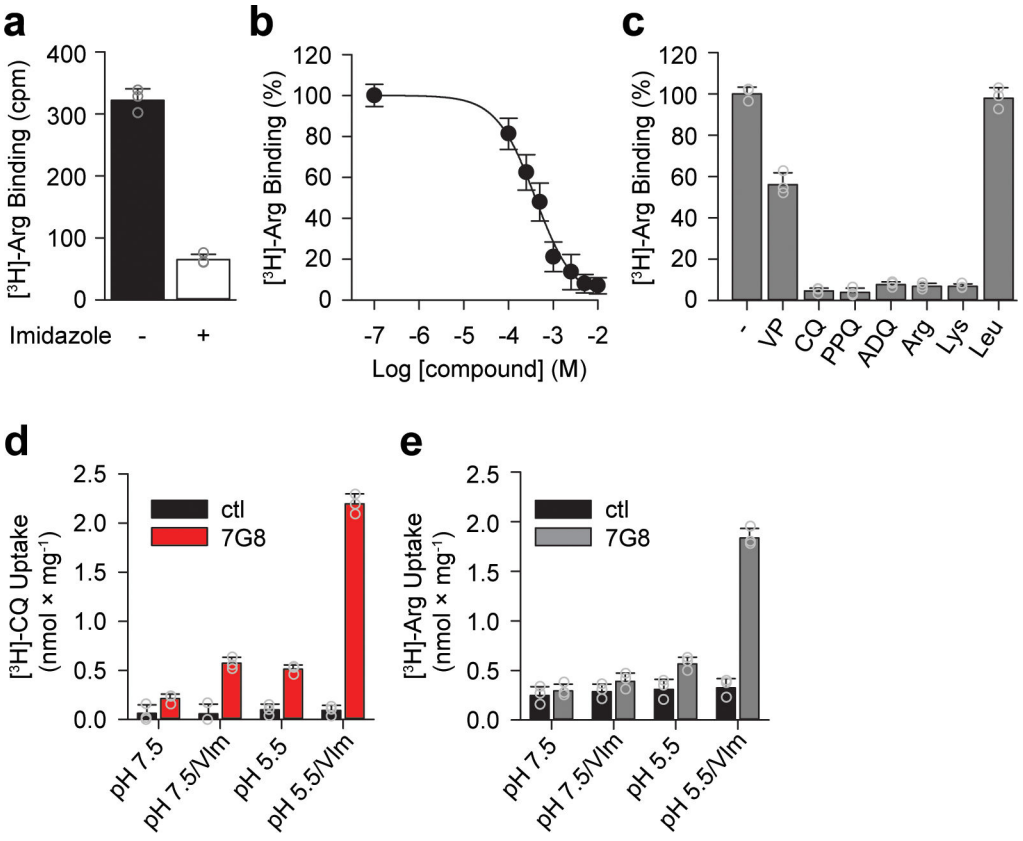

Extended Data Figure 8 |. Binding and transport assays for PfCRT 7G8.

a, Total binding of 125 nM [^{3}H]-Arg to 100 ng of nanodisc-incorporated PfCRT 7G8 was measured in the absence (−) or presence (+) of 800 mM imidazole (which competes with the His-tagged PfCRT 7G8 isoform for binding to the copper-coated YSi SPA beads). Bars show means ± SEM (N=3 independent experiments), and grey symbols show the data mean of technical replicates (n=3) of each independent experiment. **b,** Isotopic dilution of 125 nM [^{3}H]-Arg with non-radiolabeled Arg revealed a LogEC_{50} value of −3.40 ± 0.033 M (corresponding to 397 μM). We note that the primary source of Arg in parasitized red blood cells is from the proteolysis of hemoglobin, which in its native state as a tetramer is present at 5 mM[90]. Symbols show means ± SEM (N=3 independent experiments of n=3 technical replicates). **c,** Binding of 125 nM [^{3}H]-Arg in the presence or absence of 10 μM verapamil (VP), 1 μM CQ or PPQ, 0.1 μM amodiaquine (ADQ), or 1 mM Arg, Lys or Leu. Data were normalized to the signal in the absence of the respective non-radiolabeled compound and show means ± SEM (N=3 independent experiments), and grey symbols show the data mean of n=3 technical replicates of each independent experiment. **d-e**, Uptake of **(d)** 370 nM [^{3}H]-CQ or **(e)** 250 nM [^{3}H]-Arg, was measured for 1 min periods in PfCRT 7G8-containing proteoliposomes preloaded with 100 mM KP_i, pH 7.5 diluted in buffer composed of 50 mM Tris/MES, pH 5.5 or 7.5 ± the K^+ ionophore valinomycin (5 μM). The valinomycin (Vlm)-mediated K^+ efflux proceeding down its concentration gradient generated an inside-negative membrane potential. Empty liposomes lacking PfCRT 7G8 served as controls. Data show means ± SEM (N=3 independent experiments), and grey symbols show the data mean of n=3 technical replicates of each independent experiment.

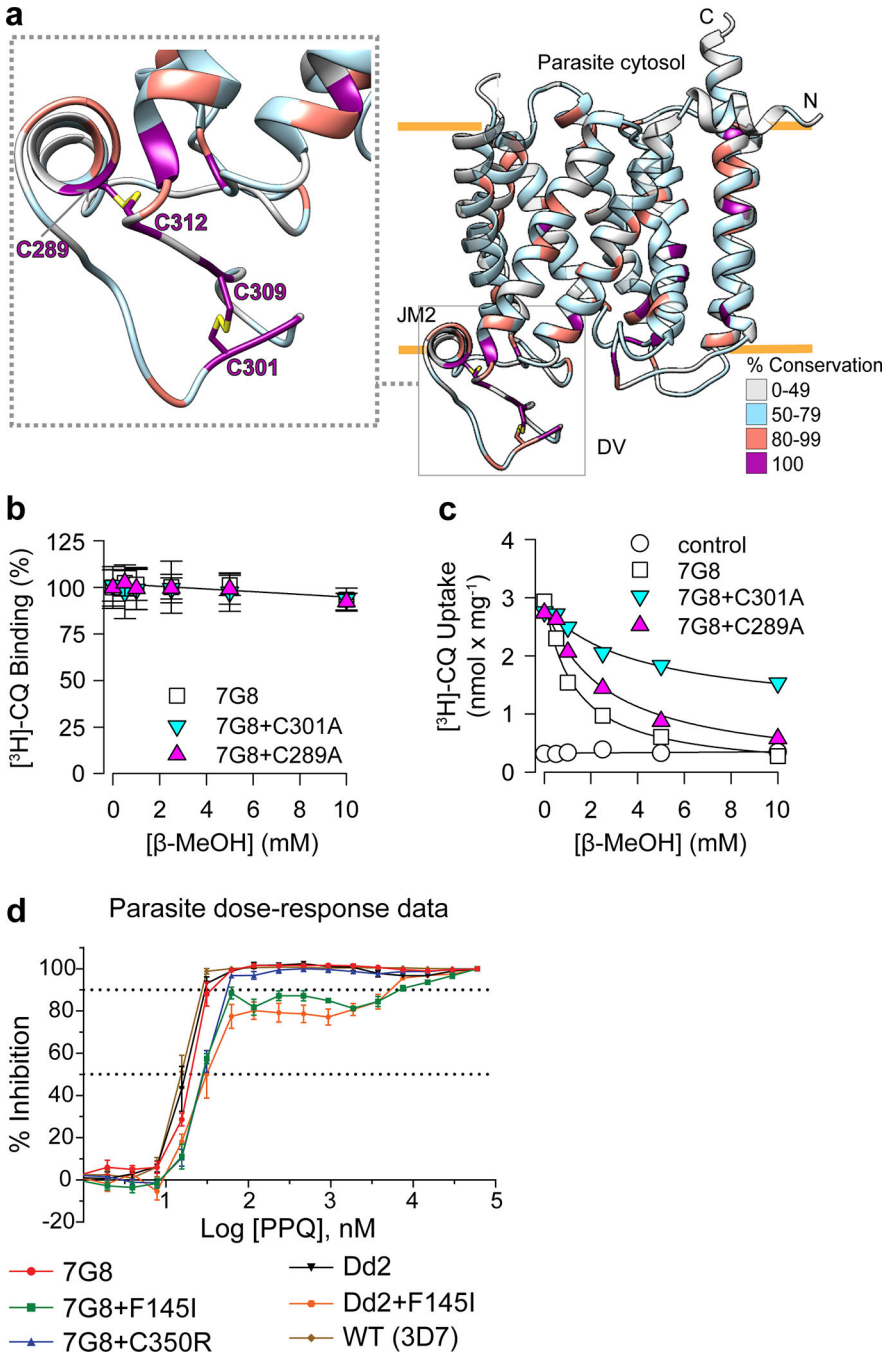

Extended Data Figure 9 |. Role of conserved Cys residues in CQ binding and transport, and Parasite PPQ dose-response data.

a, Cysteine residues that likely form disulfide bonds on the loop adjacent to JM2 and connecting to TM8 are shown in yellow and rendered as sticks. Their locations are shown as an inset of the overall structure and are colored by conservation (as per Extended Data Fig. 7). **b**, Effect of reducing conditions on the binding of [^{3}H]-CQ by PfCRT 7G8, 7G8+C289A, and 7G8+C301A. SPA binding of 100 nM [^{3}H]-CQ was performed with 200 ng of each protein variant reconstituted into nanodiscs at pH 7.5 in the presence of varying

concentrations of β-mercaptoethanol. Data (shown as means ± SEM of N=3 independent experiments of n=3 technical replicates) were normalized with regard to the activity measured for PfCRT 7G8 in the absence of the reducing agent. **c**, Effect of the reducing agent β-mercaptoethanol on [^{3}H]-CQ transport by PfCRT 7G8, 7G8+C289A, or 7G8+C301A. Uptake of 100 nM [^{3}H]-CQ was measured for 1 min periods in control liposomes and proteoliposomes containing the indicated PfCRT variants, in the presence of increasing concentrations of β-mercaptoethanol. Data show means of N=2 independent experiments performed as n=4 technical replicates and were subjected to non-linear regression fitting using hyperbolic decay models with either two (for 7G8 and 7G8+C289A) or three (including 7G8+C301A) parameters. Kinetic constants are shown as means ± SEM of the fits. The IC_{50} (concentration of β-mercaptoethanol yielding half-maximal reduction of transport) for 7G8 and 7G8+C289A were 1.24 ± 0.14 mM and 2.58 ± 0.39 mM, respectively. For 7G8+C301A the IC_{50} was 4.17 ± 0.16 mM with a remaining activity of 60.2 ± 8.2 % (compared to the activity in the absence of the reducing agent). **d**, PPQ dose-response data for *pfcrt*-edited and control parasite lines, generated from 72 h growth inhibition assays. Data are presented as means ± SEM from N=4 independent assays performed in duplicate (n=2). Statistical significance was determined via two-tailed Mann-Whitney U tests.

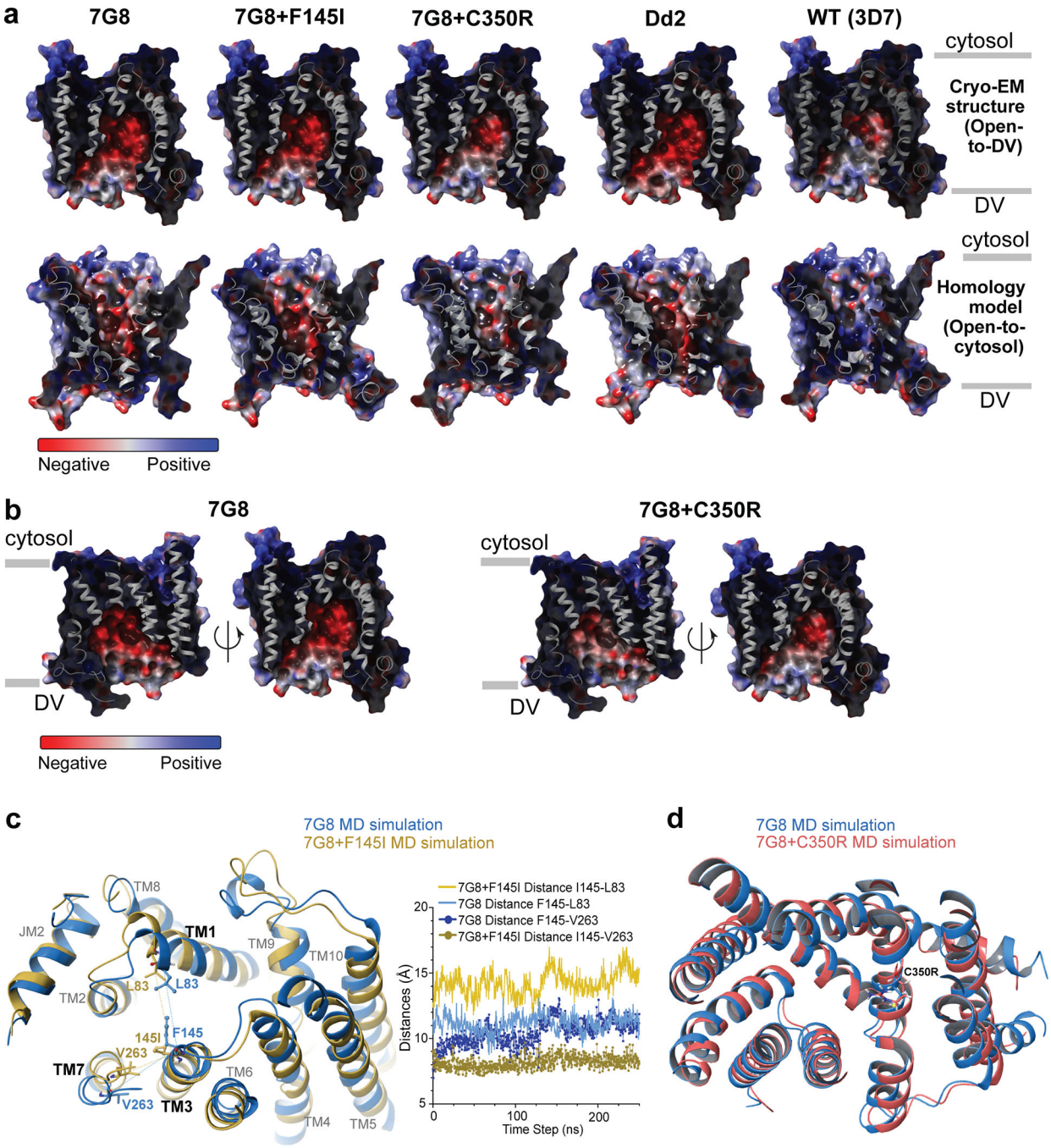

Extended Data Figure 10 |. Electrostatic potential surfaces of isoform-specific PfCRT cavities, and molecular dynamics simulations.

a, Electrostatic surfaces for the solved open-to-DV conformation for 7G8 and modeled isoforms, predicted at pH 5.5. Images are presented as a vertical slice through the transporter, showing net charges in the cavity and locations of TM helices. The row below shows the electrostatic surfaces for the homology models of these PfCRT isoforms, illustrated in their open-to-cytosol configuration, predicted at pH 7.0. **b**, Surface representation of the electrostatic potential of the central cavity of 7G8 and the 7G8+C350R

variant, shown in two different orientations with red and blue being negatively and positively charged, respectively. **c**, Molecular dynamics simulations on the 7G8 structure (minus the Fab) over 250 ns trajectories, establishing the equilibrium positions of protein side chains and distances between position 145 and residues on proximal helices. **d**, Molecular dynamics simulations on the 7G8 structure (minus the Fab) over 250 ns trajectories, establishing the equilibrium positions of protein side chains between position 350 and residues on proximal helices, and showing marginal movement between the C350 and the 350R isoforms.

Extended Data Table 1 |

Cryo-EM data collection, refinement and validation statistics.

	PfCRT with Fab-Variable Domains (EMD-20806) (PDB 6UKJ)	
Data collection and processing		
Magnification	215,000	
Voltage (kV)	300	
Electron exposure (e–/Å^2)	91.56	
Exposure time (s)	6	
Dose rate (e–/pixel/s)	4	
Defocus range (μm)	1.5 ± 0.23	
Pixel size (Å)	0.5175	
Symmetry imposed	C1	
Number of micrographs	3,377	
Initial particle images (no.)	183,241	
Final particle images (no.)	17,030	
Map resolution (Å)	3.3	
FSC threshold	0.143	
Map resolution range (Å)		
Local	2.6–5.6	
Directional	3.1–3.3	
Sphericity of 3DFSC	0.99	
Refinement	**PfCRT**	**Fab-Variable Domains**
Initial model used (PDB code)	-	4XMM
Model resolution (Å)	3.5	
FSC threshold	0.5	
Model resolution range (Å)	2.6–5.6	
Map sharpening *B* factor (Å^2)	−28.3	
Residue range	47–113 and 123–405	Heavy Chain: 4–129 Light Chain: 2–106
Model composition		
Non-hydrogen atoms	2810	1780
Protein residues	350	231
Ligands	1	0

B factors (Å^2)		
Protein	81.1	74.5
Ligand	82.5	-
R.m.s. deviations		
Bond lengths (Å)	1.272	1.162
Bond angles (°)	6.91	3.75
Validation		
MolProbity score	1.61	1.59
Clashscore	6.91	3.75
Poor rotamers (%)	0.96	0.00
EM-Ringer Score	3.49	3.53
Ramachandran plot		
Favored (%)	96.8	93.4
Allowed (%)	3.2	6.6
Disallowed (%)	0.0	0.0

Extended Data Table 2 |

Expanded list of PfCRT mutations with chloroquine and piperaquine phenotypes and binding and transport kinetics of PfCRT variants.

a, CQ, chloroquine; PPQ, piperaquine; R, resistant; S, sensitive; TM, transmembrane; mod. moderate. All mutations were identified in field isolates except for C101F that was selected under PPQ pressure in Dd2 parasites. The PfCRT 7G8 and Dd2 haplotypes are listed in Extended Data Fig. 1. The drug first listed in the Associated Phenotype column is thought to have been the driver of selection and the susceptibility status is indicated; the drug listed in parentheses shows the associated phenotype. **b,** Dissociation constants (K_d) and maximum binding constants (B_{max}) were determined with equilibrium dialysis using 4.2 pmol of the indicated PfCRT variant in 50 mM Tris/Mes, pH 7.5 or 5.5, 5 % glycerol, and 0.1 mM TCEP. Data (mean ± SEM of N=3 independent experiments) were subjected to global non-linear regression fitting in GraphPad Prism and shown as the log mean ± SEM of the fit. Transport kinetics for [^{3}H]-CQ and [^{3}H]-PPQ were determined with PfCRT variants reconstituted into proteoliposomes or with liposomes (control) using an inwardly-directed pH gradient. Data (mean of N=2 independent experiments of n=4 technical replicates) for the 1-min uptake of [^{3}H]-CQ or [^{3}H]-PPQ (depicted in Fig. 3i) are shown as for each variant tested. Data of the concentration-dependent uptake of [^{3}H]-CQ or [^{3}H]-PPQ (mean of N=2 independent experiments of n=4 technical replicates) shown in Fig. 3j were fit to the Michaelis-Menten equation in GraphPad Prism to obtain the K_m and V_{max} (shown as mean ± SEM of the fit).

a

Mutations	Origin	Associated Haplotype	Associated Phenotype	Confirmed[1]	Location	Lining the cavity	Conservation, *Plasmodium*[2]	Conservation, Apicomplexa[3]	Citation

C72S	Field	7G8	CQ-R (PPQ-S)	Yes	TM1	Yes	83%	45%	3
M74I	Field	Dd2	CQ-R (PPQ-S)	Yes	TM1	Yes	100%	55%	3
N75E	Field	Dd2	CQ-R (PPQ-S)	Yes	TM1	Yes	100%	82%	3
K76T	Field	Dd2 and 7G8	CQ-R (PPQ-S)	Yes	TM1	Yes	100%	55%	3
T93S	Field	Dd2+T93S	PPQ-R (CQ-R)	Yes	TM2	Yes	100%	64%	7,8
H97Y	Field	Dd2+H97Y	PPQ-R (CQ-R)	Yes	TM2	Yes	100%	55%	6
C101F	Lab	Dd2+C101F	PPQ-R (CQ-S)	Yes	TM2	Yes	100%	55%	12
F145I	Field	Dd2+F145I	PPQ-R (CQ-S)	Yes	TM3	Yes	67%	36%	6,28
I218F	Field	Dd2+I218F	PPQ-R (CQ-R low)	Yes	TM6	Partial	100%	55%	7,8
A220S	Field	Dd2/7G8	CQ-R (PPQ-S)	Yes	TM6	Yes	67%	55%	3
Q271E	Field	Dd2	CQ-R (PPQ-S)	Yes	TM7 - JM2	No	67%	36%	3
N326S/D	Field	Dd2/7G8	CQ-R (PPQ-S)	Yes	TM8	Yes	100%	82%	3
M343L	Field	Dd2+M343L	PPQ-R low (CQ-S)	Yes	TM9	Partial	100%	55%	6
C350R	Field	7G8+C350R	PPQ-R low (CQ-S)	Yes	TM9	Yes	100%	55%	9; this study
G353V	Field	Dd2+G353V	PPQ-R mod. (CQ-S)	Yes	TM9	Yes	100%	55%	6
I356T/L	Field	Dd2/7G8	CQ-R (PPQ-S)	Yes	TM9	Yes	100%	55%	3
R371I	Field	Dd2	CQ-R (PPQ-S)	Yes	TM9 - 10	No	67%	36%	3

b

	CQ						
	Binding at pH 7.5		Binding at pH 5.5		Transport in proteoliposomes		
Variant	K_d (μM)	B_{max} (mol CQ/mol PfCRT)	K_d (μM)	B_{max} (mol CQ/mol PfCRT)	1-min uptake (nmol × mg^{-1})	K_m (μM)	V_{max} (nmol × mg^{-1} × min^{-1})

Control	–	–	–	–	0.12 ± 0.02	n.d.*	n.d.
7G8	0.28 ± 0.06	0.38 ± 0.02	0.21 ± 0.06	0.40 ± 0.03	3.14 ± 0.50	0.77 ± 0.15	92.20 ± 4.91
7G8+F145I	0.29 ± 0.05	0.43 ± 0.02	0.24 ± 0.06	0.39 ± 0.03	0.24 ± 0.05	0.36 ± 0.08	63.01 ± 3.57
7G8+C350R	0.30 ± 0.06	0.42 ± 0.03	0.13 ± 0.03	0.37 ± 0.02	0.80 ± 0.21	1.43 ± 0.16	17.97 ± 0.87
Dd2	0.31 ± 0.04	0.38 ± 0.01	0.20 ± 0.04	0.42 ± 0.04	3.33 ± 0.22	0.64 ± 0.07	91.37 ± 2.79
WT	0.28 ± 0.04	0.42 ± 0.02	0.28 ± 0.03	0.40 ± 0.02	0.58 ± 0.08	n.d.	n.d.

	PPQ						
	Binding at pH 7.5		Binding at pH 5.5		Transport in proteoliposomes		
Variant	K_d (μM)	B_{max} (mol CQ/mol PfCRT)	K_d (μM)	B_{max} (mol CQ/mol PfCRT)	1-min uptake (nmol × mg^{-1})	K_m (μM)	V_{max} (nmol × mg^{-1} × min^{-1})
Control	–	–	–	–	0.09 ± 0.01	n.d.	n.d.
7G8	0.22 ± 0.04	0.40 ± 0.02	0.09 ± 0.02	0.40 ± 0.01	3.26 ± 0.33	n.d.	n.d.
7G8+F145I	0.26 ± 0.03	0.42 ± 0.01	0.22 ± 0.03	0.38 ± 0.01	1.41 ± 0.12	0.61 ± 0.15	109.30 ± 7.27
7G8+C350R	0.25 ± 0.04	0.41 ± 0.02	0.21 ± 0.03	0.39 ± 0.02	0.82 ± 0.07	0.53 ± 0.04	153.00 ± 3.10
Dd2	0.22 ± 0.03	0.39 ± 0.02	0.08 ± 0.01	0.39 ± 0.01	3.09 ± 0.41	n.d.	n.d.
WT	0.26 ± 0.04	0.40 ± 0.02	0.26 ± 0.04	0.38 ± 0.02	0.51 ± 0.04	n.d.	n.d.

[1] These mutations were detected in *P. falciparum* parasites from areas of PPQ resistance. However, their contribution to PPQ resistance has not been confirmed in cultured isolates or gene-edited parasite lines. For all others, the association with CQ or PPQ resistance has been observed in parasites (culture-adapted or gene edited).

[2] Percent identity of the amino acid present in *P. falciparum* wild-type (3D7) parasites, when examined across CRT orthologs from the six *Plasmodium* species listed in Extended Data Fig. 7. For *P. falciparum*, we only considered the 3D7 strain and not the CQ-resistant Dd2 and 7G8 strains.

[3] Percent identity of the amino acid present in P. *falciparum* wild-type (3D7) parasites, when examined across CRT orthologs from the six *Plasmodium* species plus the five other representative *Apicomplexan* species listed in Extended Data Fig. 7. For *P. falciparum*, we only considered the 3D7 strain and not the CQ-resistant Dd2 and 7G8 strains.

* n.d., not determined because of their low transport activities.

Extended Data Table 3 | Intracellular accumulation ratio (CAR) of [^{3}H]-CQ and [^{3}H]-PPQ, antimalarial IC_{50} values, and piperaquine survival assay (PSA) data with *pfcrt*-modified *P. falciparum* parasite lines.

Cellular accumulation ratios (CAR) indicate the mean ± SEM, determined from 4–6 independent assays performed in duplicate. CQ, chloroquine; PPQ, piperaquine; n, assay number. Statistical significance was determined via two-tailed Mann-Whitney U tests. P values are reported in comparison with the control lines 7G8^{7G8} and Dd2^{Dd2}. Cells are highlighted in grey when P<0.05. IC_{50} values (nM) indicate the mean ± SEM, as determined by 4 independent assays performed in duplicate. CQ, chloroquine; md-CQ, monodesethyl-chloroquine (the active CQ metabolite); PPQ, piperaquine. N, number of assays. Statistical significance was determined via two-tailed Mann-Whitney U tests. P values are reported for comparisons with the isogenic parasite lines 7G8^{7G8} or Dd2^{Dd2} for instances where P<0.05, highlighted in grey. Piperaquine (PPQ) survival assay values are presented as the mean ± SEM determined from 2 to 5 independent assays performed in duplicate. N, number of assays. Statistical significance was determined via two-tailed Mann-Whitney U tests. P values are reported for comparisons with the isogenic parasite lines 7G8^{7G8} for instances where P<0.05, highlighted in grey.

	7G8^{7G8}	7G8$^{7G8+F145I}$	7G8$^{7G8+C350R}$	Dd2^{Dd2}	WT (3D7)
[^{3}H]-CQ CAR	**14.5 ± 3.7**	**388.4 ± 38.9**	**406.4 ± 22.4**	**26.3 ± 2.9**	**876.7 ± 38.7**
n	4	4	4	6	4
P vs 7G8^{7G8}	–	0.03	0.03	–	–
P vs Dd2^{Dd2}	–	–	–	–	0.01
[^{3}H]-PPQ CAR	**1943.9 ± 82.2**	**1125.6 ± 59.6**	**1207.4 ± 119.8**	**1861.3 ± 91.8**	**2123.8 ± 72.2**
n	4	4	4	4	4
P vs 7G8^{7G8}	–	0.03	0.03	–	–
P vs Dd2^{Dd2}	–	–	–	–	0.03
CQ IC_{50}	**83.0 ± 7.5**	**7.3 ± 0.4**	**6.9 ± 0.3**	**142.9 ±21.8**	**12.2 ± 0.5**
N	4	4	4	4	4
P vs 7G8^{7G8}	–	0.03	0.03	–	–
P vs Dd2^{Dd2}	–	–	–	–	0.03
md-CQ IC_{50}	**919 ± 125**	**47.8 ± 2.5**	**36.5 ± 2.0**	**1796 ± 199**	**48.6 ± 3.1**
N	4	4	4	4	4
P vs 7G8^{7G8}	–	0.03	0.03	–	–
P vs Dd2^{Dd2}	–	–	–	–	0.03
PPQ IC_{50}	**21.4 ± 1.0**	**28.7 ± 1.0**	**29.5 ± 1.6**	**18.3 ± 1.9**	**16.2 ± 1.3**
N	4	4	4	4	4
P vs 7G8^{7G8}	–	0.03	0.03	–	–
P vs Dd2^{Dd2}	–	–	–	–	0.20

	$7G8^{7G8}$	$7G8^{7G8+F145I}$	$7G8^{7G8+C350R}$	$Dd2^{Dd2}$	WT (3D7)
PSA 1600 nM	**0.54 ± 0.20**	**14.7 ± 4.2**	**5.9 ± 0.9**	**0.87 ± 0.10**	**0.51 ± 0.17**
N	5	3	3	4	2
P vs $7G8^{7G8}$	–	0.04	0.04	–	–
PSA 800 nM	**0.56 ± 0.17**	**13.1 ± 3.9**	**6.6 ± 0.46**	**0.89 ± 0.16**	**0.62 ± 0.16**
N	5	3	3	4	2
P vs $7G8^{7G8}$	–	0.04	0.04	–	–
PSA 400 nM	**0.66 ± 0.20**	**12.7 ± 2.5**	**10.5 ± 1.1**	**1.1 ± 0.24**	**0.61 ± 0.19**
N	5	3	3	4	2
P vs $7G8^{7G8}$	–	0.04	0.04	–	–
PSA 200 nM	**1.4 ± 0.2**	**8.6 ± 2.4**	**9.5 ± 1.2**	**1.1 ± 0.10**	**1.2 ± 0.54**
N	5	3	3	4	2
P vs $7G8^{7G8}$	–	0.04	0.04	–	–
PSA 100 nM	**1.6 ± 0.3**	**4,0 ± 0.6**	**7.7 ± 2.5**	**1.7 ± 0.2**	**1.3 ± 0.35**
N	5	3	3	4	2
P vs $7G8^{7G8}$	–	0.04	0.04	–	–
PSA 50 nM	**4.9 ± 1.3**	**8.5 ± 1.2**	**31.8 ± 9.3**	**7.6 ± 3.3**	**4.9 ± 1.1**
N	5	3	3	4	2
P vs $7G8^{7G8}$	–	0.04	0.04	–	–
PSA 25 nM	**48.3 ± 5.5**	**44.5 ± 2.4**	**62.1 ± 9.6**	**35.3 ± 12.2**	**11.0 ± 1.7**
N	5	3	3	4	2
P vs $7G8^{7G8}$	–	0.79	0.25	–	–
PSA 12.5 nM	**76.7 ± 5.1**	**62.3 ± 4.1**	**79.8 ± 5.5**	**67.7 ± 11.9**	**7.2 ± 1.5**
N	5	3	3	4	2
P vs $7G8^{7G8}$	–	0.07	0.79	–	–
PSA 6.25 nM	**87.1 ± 3.5**	**83.4 ± 4.5**	**90.7 ± 5.1**	**83.6 ± 6.1**	**12.1 ± 6.8**
N	5	3	3	4	2
P vs $7G8^{7G8}$	–	0.07	0.79	–	–
PSA 3.125 nM	**93.8 ± 3.5**	**95.7 ± 3.1**	**96.6 ± 2.4**	**95.9 ± 2.1**	**81.2 ± 19.6**
N	5	3	3	4	2
P vs $7G8^{7G8}$	–	0.07	0.79	–	–

Supplementary Material

Refer to Web version on PubMed Central for supplementary material.

Acknowledgments

We thank Bill Rice, Ed Eng, Laura Kim, Kelsey Jordan, Misha Kopylov, Venkat Dandey, Hui Wei, Sargis Dallakyan, Carl Negro, Stanislaw Gabryszewski, Somnath Mukherjee, Bryce Riegel, Oliver Clarke and Yunting Chen for their helpful contributions. This work was supported by NIH grants (R01 AI147628 to F.M., D.A.F., and M.Q.; R35 GM132120 and R01 AI147628 to F.M.; R37 AI50234 and R01 AI124678 to D.A.F.; R01 GM119396 to M.Q.; R01 AI506312 and AI111962 to P.D.R.; R01 GM117372 to A.A.K.; T32 HL120826 to J.K.; P41 GM103310 to C.S.P. and B.C.; the Agency for Science, Technology and Research Singapore (to Y.Z.T.); the Simons Foundation (SF349247 to C.S.P. and B.C.); and NYSTAR (to C.S.P. and B.C.). Some of the work was performed at the Center for Membrane Protein Production and Analysis (COMPPÅ; P41 GM116799 to Wayne Hendrickson) and at the National Resource for Automated Molecular Microscopy at the Simons Electron Microscopy Center (P41 GM103310), both located at the New York Structural Biology Center.

References

1. Su XZ, Lane KD, Xia L, Sa JM & Wellems TE *Plasmodium* genomics and genetics: new insights into malaria pathogenesis, drug resistance, epidemiology, and evolution. Clin. Microbiol. Rev 32, e00019–00019 (2019). [PubMed: 31366610]
2. van der Pluijm RW et al. Determinants of dihydroartemisinin-piperaquine treatment failure in *Plasmodium falciparum* malaria in Cambodia, Thailand, and Vietnam: a prospective clinical, pharmacological, and genetic study. Lancet Infect Dis 19, 952–961 (2019). [PubMed: 31345710]
3. Fidock DA et al. Mutations in the *P. falciparum* digestive vacuole transmembrane protein PfCRT and evidence for their role in chloroquine resistance. Mol. Cell 6, 861–871 (2000). [PubMed: 11090624]
4. Martin RE et al. Chloroquine transport via the malaria parasite's chloroquine resistance transporter. Science 325, 1680–1682 (2009). [PubMed: 19779197]
5. Blasco B, Leroy D & Fidock DA Antimalarial drug resistance: linking *Plasmodium falciparum* parasite biology to the clinic. Nat. Med. 23, 917–928 (2017). [PubMed: 28777791]
6. Ross LS et al. Emerging Southeast Asian PfCRT mutations confer Plasmodium falciparum resistance to the first-line antimalarial piperaquine. Nat. Commun 9, 3314 (2018). [PubMed: 30115924]
7. Hamilton WL et al. Evolution and expansion of multidrug-resistant malaria in southeast Asia: a genomic epidemiology study. Lancet Infect Dis 19, 943–951 (2019). [PubMed: 31345709]
8. Dhingra SK, Small-Saunders JL, Ménard D & Fidock DA (2019). Plasmodium falciparum piperaquine resistance driven by PfCRT. Lancet Infect. Dis (in press).
9. Pelleau S et al. Adaptive evolution of malaria parasites in French Guiana: Reversal of chloroquine resistance by acquisition of a mutation in *pfcrt*. Proc. Natl. Acad. Sci. USA 112, 11672–11677 (2015). [PubMed: 26261345]
10. World Health Organization. World Malaria Report 2018. https://www.who.int/malaria/publications/world-malaria-report-2018/en (2018).
11. Sullivan DJ Jr. Quinolines block every step of malaria heme crystal growth. Proc. Natl. Acad. Sci. USA 114, 7483–7485 (2017). [PubMed: 28696317]
12. Dhingra SK et al. A variant PfCRT isoform can contribute to Plasmodium falciparum resistance to the first-line partner drug piperaquine. MBio 8, e00303–17 (2017). [PubMed: 28487425]
13. Lakshmanan V et al. A critical role for PfCRT K76T in *Plasmodium falciparum* verapamil-reversible chloroquine resistance. EMBO J. 24, 2294–2305 (2005). [PubMed: 15944738]
14. Sanchez CP et al. Differences in trans-stimulated chloroquine efflux kinetics are linked to PfCRT in *Plasmodium falciparum*. Mol. Microbiol 64, 407–420 (2007). [PubMed: 17493125]
15. Paguio MF, Cabrera M & Roepe PD Chloroquine transport in *Plasmodium falciparum*. 2. Analysis of PfCRT-mediated drug transport using proteoliposomes and a fluorescent chloroquine probe. Biochemistry 48, 9482–9491 (2009). [PubMed: 19725576]
16. Sanchez CP et al. Phosphomimetic substitution at Ser-33 of the chloroquine resistance transporter PfCRT reconstitutes drug responses in *Plasmodium falciparum*. J. Biol. Chem 294: 12766–12778 (2019). [PubMed: 31285265]
17. Renaud JP et al. Cryo-EM in drug discovery: achievements, limitations and prospects. Nat. Rev. Drug Discov 17, 471–492 (2018). [PubMed: 29880918]

18. Dominik PK et al. Conformational chaperones for structural studies of membrane proteins using antibody phage display with nanodiscs. Structure 24, 300–309 (2016). [PubMed: 26749445]
19. Callaghan PS, Hassett MR & Roepe PD Functional comparison of 45 naturally occurring isoforms of the *Plasmodium falciparum* chloroquine resistance transporter (PfCRT). Biochemistry 54, 5083–5094 (2015). [PubMed: 26208441]
20. Quick M & Javitch JA Monitoring the function of membrane transport proteins in detergent-solubilized form. Proc. Natl. Acad. Sci. USA 104, 3603–3608 (2007). [PubMed: 17360689]
21. Lekostaj JK, Natarajan JK, Paguio MF, Wolf C & Roepe PD Photoaffinity labeling of the *Plasmodium falciparum* chloroquine resistance transporter with a novel perfluorophenylazido chloroquine. Biochemistry 47, 10394–10406 (2008). [PubMed: 18767816]
22. Bellanca S et al. Multiple drugs compete for transport via the *Plasmodium falciparum* chloroquine resistance transporter at distinct but interdependent sites. J. Biol. Chem 289, 36336–36351 (2014). [PubMed: 25378409]
23. Sa JM et al. Geographic patterns of *Plasmodium falciparum* drug resistance distinguished by differential responses to amodiaquine and chloroquine. Proc. Natl. Acad. Sci. USA 106, 18883–18889 (2009). [PubMed: 19884511]
24. Shi L, Quick M, Zhao Y, Weinstein H & Javitch JA The mechanism of a neurotransmitter:sodium symporter--inward release of Na+ and substrate is triggered by substrate in a second binding site. Mol. Cell 30, 667–677 (2008). [PubMed: 18570870]
25. Juge N et al. *Plasmodium falciparum* chloroquine resistance transporter is a H+-coupled polyspecific nutrient and drug exporter. Proc. Natl. Acad. Sci. USA 112, 3356–3361 (2015). [PubMed: 25733858]
26. Kuhn Y, Rohrbach P & Lanzer M Quantitative pH measurements in *Plasmodium falciparum*-infected erythrocytes using pHluorin. Cell Microbiol. 9, 1004–1013 (2007). [PubMed: 17381432]
27. Ashcroft F, Gadsby D & Miller C The blurred boundary between channels and transporters. Philos. Trans. R Soc. Lond. B Biol. Sci 364, 145–147 (2009). [PubMed: 18957372]
28. Agrawal S et al. Association of a novel mutation in the *Plasmodium falciparum* chloroquine resistance transporter with decreased piperaquine sensitivity. J. Infect. Dis. 216, 468–476 (2017). [PubMed: 28931241]
29. Bopp S et al. Plasmepsin II-III copy number accounts for bimodal piperaquine resistance among Cambodian Plasmodium falciparum. Nat. Commun 9, 1769 (2018). [PubMed: 29720620]
30. Duru V et al. Plasmodium falciparum dihydroartemisinin-piperaquine failures in Cambodia are associated with mutant K13 parasites presenting high survival rates in novel piperaquine in vitro assays: retrospective and prospective investigations. BMC Med. 13, 305 (2015). [PubMed: 26695060]

Extended Data References

31. Assur Z, Hendrickson WA & Mancia F Tools for coproducing multiple proteins in mammalian cells. Methods Mol. Biol 801, 173–187 (2012). [PubMed: 21987254]
32. Kawate T & Gouaux E Fluorescence-detection size-exclusion chromatography for precrystallization screening of integral membrane proteins. Structure 14, 673–681 (2006). [PubMed: 16615909]
33. Goehring A et al. Screening and large-scale expression of membrane proteins in mammalian cells for structural studies. Nat. Protoc 9, 2574–2585 (2014). [PubMed: 25299155]
34. Gibson DG et al. Enzymatic assembly of DNA molecules up to several hundred kilobases. Nat. Methods 6, 343 (2009). [PubMed: 19363495]
35. Wright DJ, O'Reilly M & Tisi D Engineering and purification of a thermostable, high-yield, variant of PfCRT, the *Plasmodium falciparum* chloroquine resistance transporter. Protein. Expr. Purif 141, 7–18 (2018). [PubMed: 28823509]
36. Paduch M et al. Generating conformation-specific synthetic antibodies to trap proteins in selected functional states. Methods 60, 3–14 (2013). [PubMed: 23280336]
37. Dominik PK & Kossiakoff AA Phage display selections for affinity reagents to membrane proteins in nanodiscs. Methods Enzymol. 557, 219–245 (2015). [PubMed: 25950967]

38. Fellouse FA, Wiesmann C & Sidhu SS Synthetic antibodies from a four-amino-acid code: a dominant role for tyrosine in antigen recognition. Proc. Natl. Acad. Sci. USA 101, 12467–12472 (2004). [PubMed: 15306681]
39. Fellouse FA et al. High-throughput generation of synthetic antibodies from highly functional minimalist phage-displayed libraries. J. Mol. Biol 373, 924–940 (2007). [PubMed: 17825836]
40. Suloway C et al. Automated molecular microscopy: the new Leginon system. J. Struct. Biol 151, 41–60 (2005). [PubMed: 15890530]
41. Lander GC et al. Appion: an integrated, database-driven pipeline to facilitate EM image processing. J. Struct. Biol 166, 95–102 (2009). [PubMed: 19263523]
42. Scheres SH RELION: implementation of a Bayesian approach to cryo-EM structure determination. J. Struct. Biol 180, 519–530 (2012). [PubMed: 23000701]
43. Kimanius D, Forsberg BO, Scheres SH & Lindahl E Accelerated cryo-EM structure determination with parallelisation using GPUs in RELION-2. Elife 5, e18722 (2016). [PubMed: 27845625]
44. Cheng A et al. High resolution single particle cryo-electron microscopy using beam-image shift. J. Struct. Biol. 204, 270–275 (2018). [PubMed: 30055234]
45. Rice WJ et al. Routine determination of ice thickness for cryo-EM grids. J. Struct. Biol. 204, 38–44 (2018). [PubMed: 29981485]
46. Zheng SQ et al. MotionCor2: anisotropic correction of beam-induced motion for improved cryo-electron microscopy. Nat. Methods 14, 331–332 (2017). [PubMed: 28250466]
47. Rohou A & Grigorieff N CTFFIND4: Fast and accurate defocus estimation from electron micrographs. J. Struct. Biol 192, 216–221 (2015). [PubMed: 26278980]
48. Zhang K Gctf: Real-time CTF determination and correction. J. Struct. Biol 193, 1–12 (2016). [PubMed: 26592709]
49. Voss NR, Yoshioka CK, Radermacher M, Potter CS & Carragher B DoG Picker and TiltPicker: software tools to facilitate particle selection in single particle electron microscopy. J. Struct. Biol 166, 205–213 (2009). [PubMed: 19374019]
50. Punjani A, Rubinstein JL, Fleet DJ & Brubaker MA cryoSPARC: algorithms for rapid unsupervised cryo-EM structure determination. Nat. Methods 14, 290–296 (2017). [PubMed: 28165473]
51. Grant T & Grigorieff N Automatic estimation and correction of anisotropic magnification distortion in electron microscopes. J. Struct. Biol 192, 204–208 (2015). [PubMed: 26278979]
52. Grant T, Rohou A & Grigorieff N cisTEM, user-friendly software for single-particle image processing. Elife 7, e35383 (2018). [PubMed: 29513216]
53. Adams PD et al. PHENIX: a comprehensive Python-based system for macromolecular structure solution. Acta Crystallogr. D Biol. Crystallogr 66, 213–221 (2010). [PubMed: 20124702]
54. Pettersen EF et al. UCSF Chimera--a visualization system for exploratory research and analysis. J. Comput. Chem 25, 1605–1612 (2004). [PubMed: 15264254]
55. Wang RY-R et al. Automated structure refinement of macromolecular assemblies from cryo-EM maps using Rosetta. Elife 5, e17219 (2016). [PubMed: 27669148]
56. Emsley P & Cowtan K Coot: model-building tools for molecular graphics. Acta Crystallogr. D Biol. Crystallogr 60, 2126–2132 (2004). [PubMed: 15572765]
57. Stuwe T et al. Nuclear pores. Architecture of the nuclear pore complex coat. Science 347, 1148–1152 (2015). [PubMed: 25745173]
58. Chen VB et al. MolProbity: all-atom structure validation for macromolecular crystallography. Acta Crystallogr. D Biol. Crystallogr 66, 12–21 (2010). [PubMed: 20057044]
59. Barad BA et al. EMRinger: side chain-directed model and map validation for 3D cryo-electron microscopy. Nat. Methods 12, 943–946 (2015). [PubMed: 26280328]
60. Kucukelbir A, Sigworth FJ & Tagare HD Quantifying the local resolution of cryo-EM density maps. Nat. Methods 11, 63–65 (2014). [PubMed: 24213166]
61. Tan YZ et al. Addressing preferred specimen orientation in single-particle cryo-EM through tilting. Nat. Methods 14, 793–796 (2017). [PubMed: 28671674]

62. Rosenthal PB & Henderson R Optimal determination of particle orientation, absolute hand, and contrast loss in single-particle electron cryomicroscopy. J. Mol. Biol 333, 721–745 (2003). [PubMed: 14568533]
63. Ludtke SJ, Baldwin PR & Chiu W EMAN: semiautomated software for high-resolution single-particle reconstructions. J. Struct. Biol. 128, 82–97 (1999). [PubMed: 10600563]
64. Voss NR & Gerstein M 3V: cavity, channel and cleft volume calculator and extractor. Nucleic Acids Res. 38, W555–562 (2010). [PubMed: 20478824]
65. Holm L & Laakso LM Dali server update. Nucleic Acids Res. 44, W351–355 (2016). [PubMed: 27131377]
66. Parker JL & Newstead S Structural basis of nucleotide sugar transport across the Golgi membrane. Nature 551, 521–524 (2017). [PubMed: 29143814]
67. Tsuchiya H et al. Structural basis for amino acid export by DMT superfamily transporter YddG. Nature 534, 417–420 (2016). [PubMed: 27281193]
68. Lee Y et al. Structure of the triose-phosphate/phosphate translocator reveals the basis of substrate specificity. Nat. Plants 3, 825–832 (2017). [PubMed: 28970497]
69. Nji E, Gulati A, Qureshi AA, Coincon M & Drew D Structural basis for the delivery of activated sialic acid into Golgi for sialyation. Nat. Struct. Mol. Biol 26, 415–423 (2019). [PubMed: 31133698]
70. Ahuja S & Whorton MR Structural basis for mammalian nucleotide sugar transport. Elife 8, e45221 (2019). [PubMed: 30985278]
71. Chen F, Mackey AJ, Stoeckert CJ Jr. & Roos DS OrthoMCL-DB: querying a comprehensive multi-species collection of ortholog groups. Nucleic Acids Res. 34, D363–368 (2006). [PubMed: 16381887]
72. Edgar RC MUSCLE: multiple sequence alignment with high accuracy and high throughput. Nucleic Acids Res. 32, 1792–1797 (2004). [PubMed: 15034147]
73. Robert X & Gouet P Deciphering key features in protein structures with the new ENDscript server. Nucleic Acids Res. 42, W320–324 (2014). [PubMed: 24753421]
74. Sastry GM, Adzhigirey M, Day T, Annabhimoju R & Sherman W Protein and ligand preparation: parameters, protocols, and influence on virtual screening enrichments. J. Comput. Aided Mol. Des 27, 221–234 (2013). [PubMed: 23579614]
75. Jacobson MP et al. A hierarchical approach to all-atom protein loop prediction. Proteins 55, 351–367 (2004). [PubMed: 15048827]
76. Lomize MA, Pogozheva ID, Joo H, Mosberg HI & Lomize AL OPM database and PPM web server: resources for positioning of proteins in membranes. Nucleic Acids Res. 40, D370–376 (2012). [PubMed: 21890895]
77. Bowers KJ. Scalable algorithms for molecular dynamics simulations on commodity clusters; Proceedings of the ACM/IEEE Conference on Supercomputing (SC06); 2006.
78. Liao J et al. Structural insight into the ion-exchange mechanism of the sodium/calcium exchanger. Science 335, 686–690 (2012). [PubMed: 22323814]
79. Mancusso R, Gregorio GG, Liu Q & Wang DN Structure and mechanism of a bacterial sodium-dependent dicarboxylate transporter. Nature 491, 622–626 (2012). [PubMed: 23086149]
80. Forrest LR Structural biology. (Pseudo-)symmetrical transport. Science 339, 399–401 (2013). [PubMed: 23349276]
81. Straimer J et al. Site-specific genome editing in *Plasmodium falciparum* using engineered zinc-finger nucleases. Nat. Methods 9, 993–998 (2012). [PubMed: 22922501]
82. Sanchez CP, Stein W & Lanzer M Trans stimulation provides evidence for a drug efflux carrier as the mechanism of chloroquine resistance in *Plasmodium falciparum*. Biochemistry 42, 9383–9394 (2003). [PubMed: 12899625]
83. Saliba KJ, Horner HA & Kirk K Transport and metabolism of the essential vitamin pantothenic acid in human erythrocytes infected with the malaria parasite *Plasmodium falciparum*. J. Biol. Chem. 273, 10190–10195 (1998). [PubMed: 9553068]
84. Dhingra SK et al. Global spread of mutant PfCRT and its pleiotropic impact on Plasmodium falciparum multidrug resistance and fitness. MBio 10, e02731–18 (2019). [PubMed: 31040246]

85. Quick M, Shi L, Zehnpfennig B, Weinstein H & Javitch JA Experimental conditions can obscure the second high-affinity site in LeuT. Nat. Struct. Mol. Biol 19, 207–211 (2012). [PubMed: 22245968]

86. Miller KR et al. T cell receptor-like recognition of tumor *in vivo* by synthetic antibody fragment. PLoS One 7, e43746 (2012). [PubMed: 22916301]

87. Wu TT & Kabat EA An analysis of the sequences of the variable regions of Bence Jones proteins and myeloma light chains and their implications for antibody complementarity. J. Exp. Med 132, 211–250 (1970). [PubMed: 5508247]

88. Hohn M et al. SPARX, a new environment for Cryo-EM image processing. J. Struct. Biol 157, 47–55 (2007). [PubMed: 16931051]

89. Wallace AC, Laskowski RA & Thornton JM LIGPLOT: a program to generate schematic diagrams of protein-ligand interactions. Protein Eng. 8, 127–134 (1995). [PubMed: 7630882]

90. Francis SE, Sullivan DJ Jr. & Goldberg DE Hemoglobin metabolism in the malaria parasite *Plasmodium falciparum*. Annu. Rev. Microbiol 51, 97–123 (1997). [PubMed: 9343345]

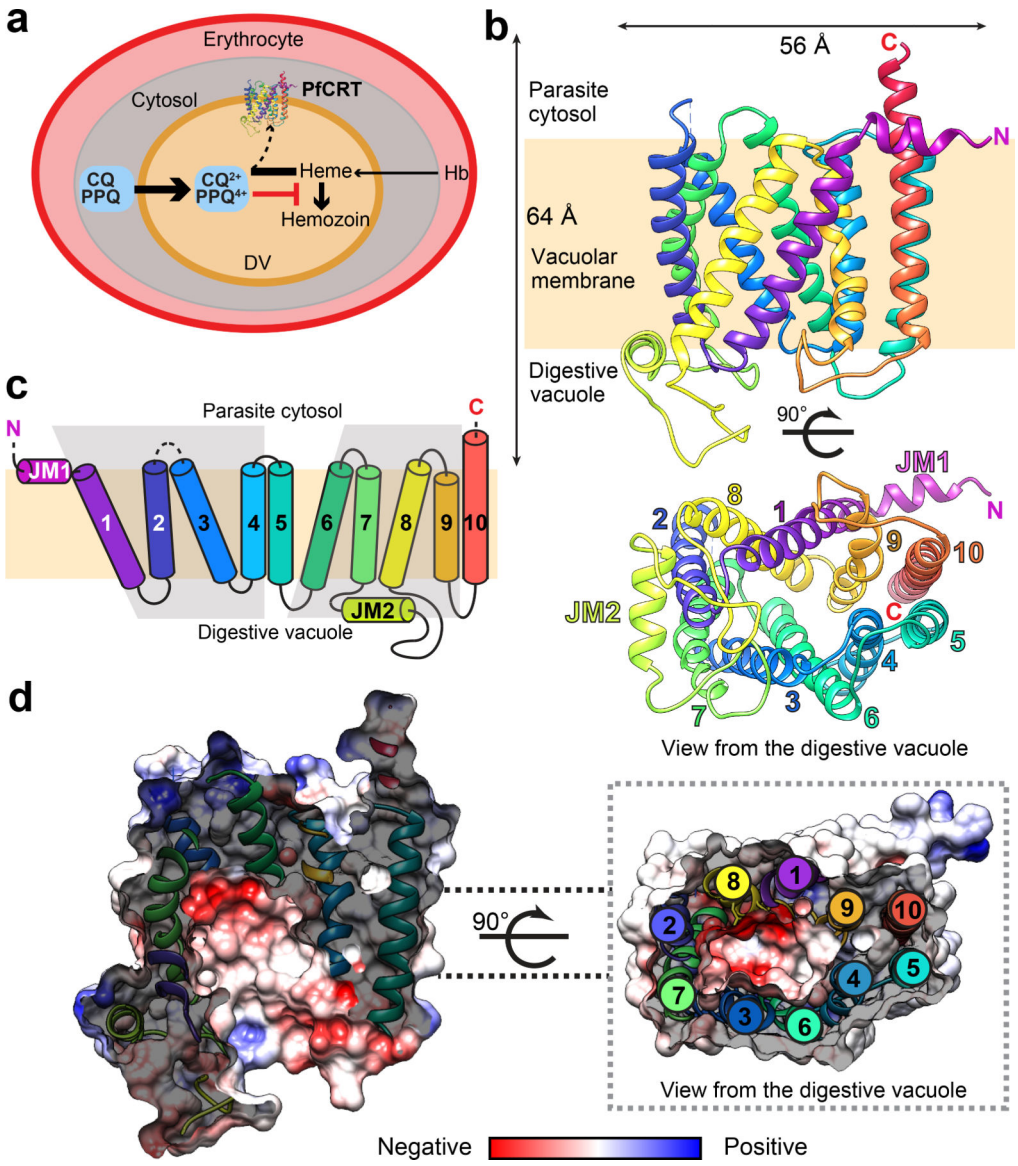

Figure 1 |. Single-particle cryo-EM structure of PfCRT 7G8.

a, PfCRT (PlasmoDB PF3D7_0709000) is localized within the membrane of the *P. falciparum* intra-erythrocytic parasite's digestive vacuole (DV), wherein imported host hemoglobin (Hb) is catabolized and toxic free heme is released. Chloroquine (CQ) and piperaquine (PPQ) are believed to concentrate in the DV as protonated species (CQ^{2+} and PPQ^{4+}) that bind heme and prevent its incorporation into non-toxic hemozoin[5]. In CQ-R parasites, PfCRT is thought to efflux CQ out of the DV into the cytosol away from its heme target. **b,** The 3.2 Å cryo-EM structure of PfCRT 7G8, with the 10 transmembrane (TM) helices colored in rainbow. The N- and C- termini are labeled. The lower panel shows a 90° rotation with helices numbered, as viewed from the DV side. **c,** Topology of PfCRT highlighting the inverted antiparallel repeats of TM 1–4 and TM 6–9 (grey). Disordered regions are shown as dotted lines. TM helices are numbered 1 to 10 (with 1–4 and 6–9 surrounding the central cavity), while the juxtamembrane helices (JM) are labeled JM1 and

JM2. **d,** Surface representation of the electrostatic potential of the central cavity with red and blue being negatively and positively charged, respectively. On the right, a central slice through the structure (dotted lines) as an insert shows the arrangement of TM helices, labeled from N- to C-terminus.

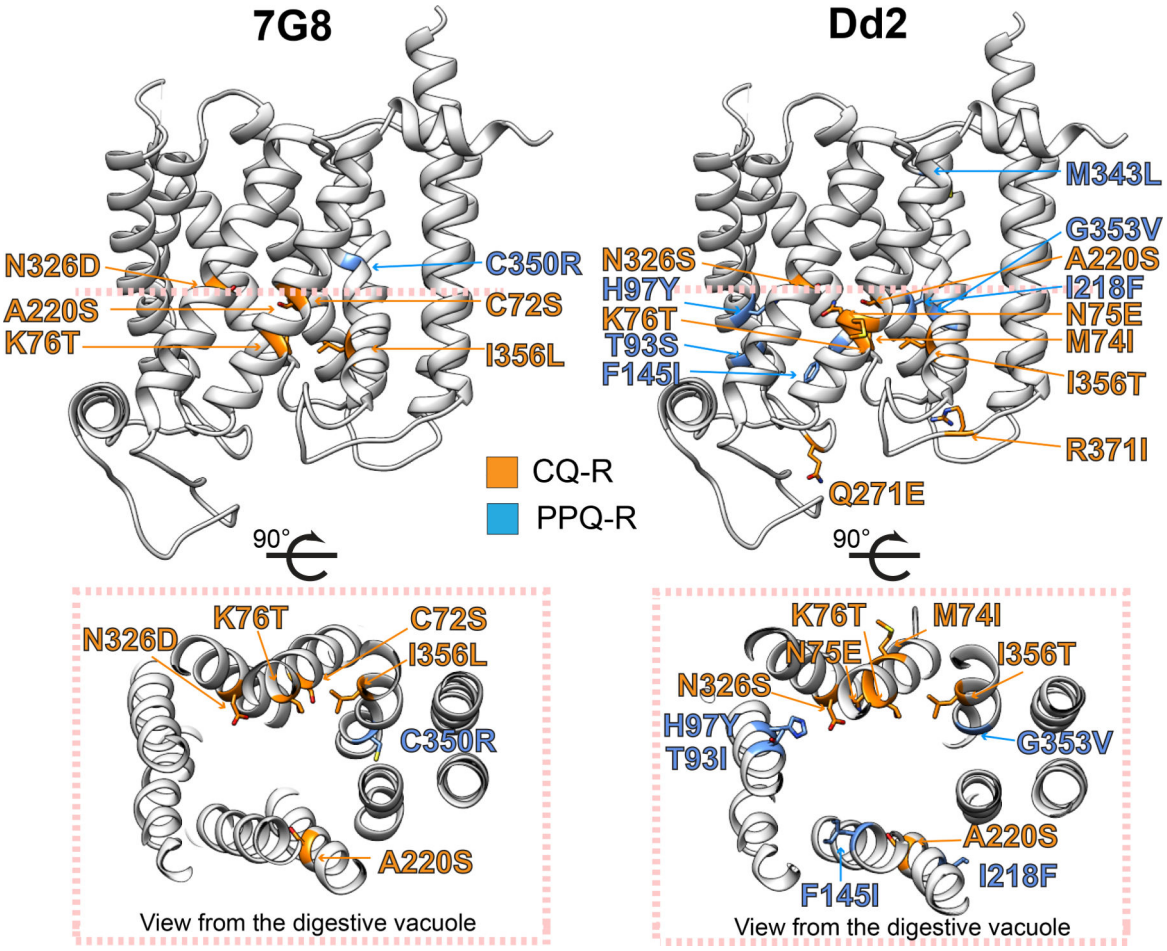

Figure 2 |. Mapping of drug-resistance mutations onto the PfCRT structure.

Residues known to contribute to resistance to CQ and PPQ (Extended Data Fig. 1; Extended Data Table 2) are mapped onto the 7G8 structure and a model of Dd2. Mutations have their side chains rendered as sticks and are colored based on their associated resistance profiles. The remaining structures are rendered in cartoon and colored in grey. Views are shown vertically (DV to the bottom) and from the DV side.

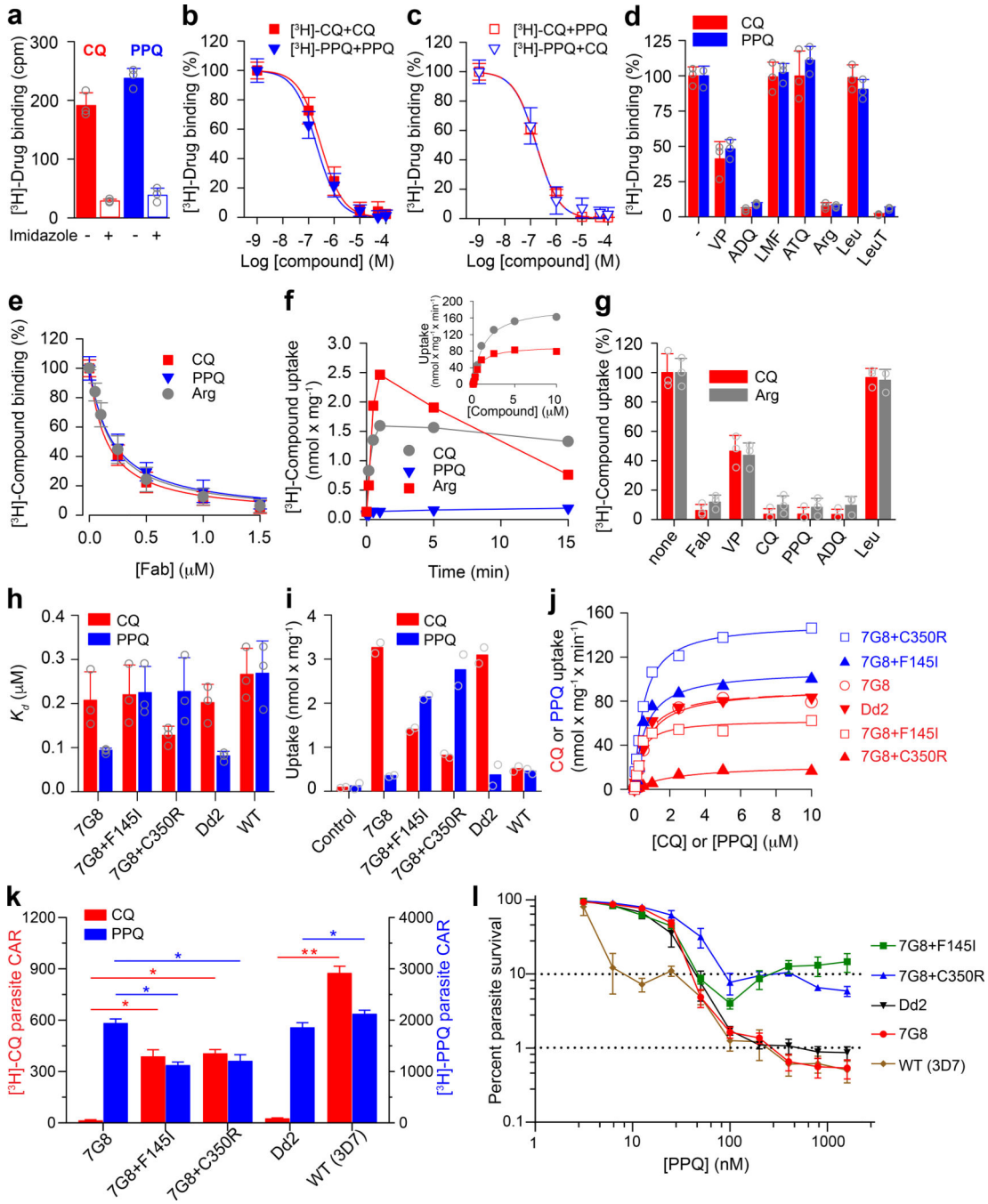

Figure 3 |. Functional characterization of PfCRT isoforms.

a, Binding of 370 nM [^{3}H]-CQ (red) or 75 nM [^{3}H]-PPQ (blue) to PfCRT 7G8 ± imidazole (bars show means ± SEM of N=3 independent experiments, and grey symbols are the data mean of technical replicates (n=3) of each independent experiment to show the distribution of the data). **b,** Isotopic dilution of [^{3}H]-CQ or [^{3}H]-PPQ revealed LogEC_{50} of −6.53 ± 0.04 M and −6.70 ± 0.05 M (corresponding to means of 297 nM for CQ and 190 nM for PPQ), respectively. Data show means ± SEM of N=3 independent experiments performed as technical replicates (n=3). **c,** Competition of [^{3}H]-CQ or [^{3}H]-PPQ binding with non-

radiolabeled PPQ or CQ, respectively, revealed LogIC_{50} values of −6.77 ± 0.03 M and −6.78 ± 0.06 M (corresponding to means of 171 nM and 167 nM), respectively. Data show means ± SEM of N=3 independent experiments performed as technical replicates (n=3). **d,** Specific binding of [^{3}H]-CQ or [^{3}H]-PPQ performed in the absence (−) or presence of 10 μM verapamil (VP), 1 μM amodiaquine (ADQ), 10 μM lumefantrine (LMF) or atovaquone (ATQ), or 1 mM Arg or Leu. Nanodiscs containing LeuT[24] served as controls. Bars show means ± SEM; N=3 independent experiments, and grey symbols show the data mean of technical replicates (n=3) of each independent experiment. **e,** Fab binding to the PfCRT 7G8 isoform reduces binding of 370 nM [^{3}H]-CQ, 75 nM [^{3}H]-PPQ, or 250 nM [^{3}H]-Arg, in a concentration-dependent manner, yielding IC_{50} values of 0.15 ± 0.02 μM, 0.20 ± 0.02 μM, or 0.18 ± 0.02 μM, respectively. Data show means ± SEM; N=3 independent experiments of technical replicates (n=3). **f,** Time course of 93 nM [^{3}H]-CQ, 75 nM [^{3}H]-PPQ, or 125 nM [^{3}H]-Arg, uptake measured with 7G8 PfCRT-containing proteoliposomes (PLs). Data show means ± SEM of N=2 independent experiments performed as n=3 technical replicates. *Inset:* transport kinetics of PfCRT-7G8 for [^{3}H]-CQ and [^{3}H]-Arg in PLs revealed Michaelis-Menten constants (K_m) of 0.77 ± 0.15 μM and 1.30 ± 0.20 μM with a maximum velocity of transport (V_{max}) of 92.2 ± 4.9 nmol x mg^{-1} x min^{-1} and 189.2 ± 9.1 nmol x mg^{-1} x min^{-1} for the uptake of CQ and Arg, respectively. Data show means of N=2 independent experiments of technical replicates (n=4) and the kinetic constants represent the means ± SEM of the global fits. **g,** Uptake of 370 nM [^{3}H]-CQ or 250 nM [^{3}H]-Arg was measured for 1 min in the presence or absence of 1 μM Fab, 10 μM VP, CQ, PPQ, ADQ, or 1 mM Leu. Values were normalized to the signal in the absence of non-radiolabeled compound. Bars show means ± SEM of N=3 independent experiments, and grey symbols show the data mean of technical replicates (n=3) of each independent experiment. Data in panel a - e are normalized to the specific signal (total counts per minute minus counts per minute in the presence of imidazole) in the absence of the respective non-radiolabeled compound. **h,** Saturation binding of [^{3}H]-CQ (red) or [^{3}H]-PPQ (blue) by indicated PfCRT variants reconstituted in nanodiscs was performed using equilibrium dialysis at pH 5.5. Dissociation constants (K_d) are shown as means ± SEM calculated from global non-linear regression fitting (N=3 independent experiments). **i,** Uptake of 100 nM [^{3}H]-CQ (red) or [^{3}H]-PPQ (blue) was measured for 1 min in proteoliposomes containing the indicated PfCRT variants or in control liposomes. Bars show means of N=2 independent experiments. Grey symbols show the data mean of technical replicates (n=4) of each independent experiment. **j,** Kinetic characterization of [^{3}H]-CQ (red) or [^{3}H]-PPQ (blue) uptake in proteoliposomes containing the indicated PfCRT variants. The initial rate of transport was measured for periods of 3 seconds using [^{3}H]-CQ or [^{3}H]-PPQ concentrations ranging from 0.05 – 10 μM. Data (means of N=2 independent experiments of technical replicates (n=4)) were fitted to the Michaelis-Menten equation. The K_m and V_{max} values are shown as means ± SEM of the fit in Extended Data Table 4. Transport kinetics of PfCRT 7G8, Dd2, or WT for PPQ or PfCRT WT for CQ were not determined due to low signal-to-noise ratios. **k,** [^{3}H]-CQ and [^{3}H]-PPQ cellular accumulation ratios (CARs) at t=60 min for edited and reference parasite lines. Data are presented as means ± SEM where N=4–6 independent experiments performed in duplicate (n=2). *P<0.05; **P<0.01 (using two-tailed Mann-Whitney U tests). **l,** Percent parasite survival of *pfcrt*-edited and reference lines following exposure to PPQ for 48 h. Percent survival was calculated for each line by dividing the parasitemia of the PPQ-treated

parasites with that of the no-drug control. Data are presented as means ± SEM where N=2–5 independent assays performed in duplicate (n=2). Statistical significance was determined via two-tailed Mann-Whitney U tests where N>2.